



Universitat Politècnica de Catalunya

DESIGN, IMPLEMENTATION AND VERIFICATION OF CUBESAT SYSTEMS FOR EARTH OBSERVATION

A Master's Thesis submitted to the Faculty of the Escola Técnica Superior
d'Enginyeria de Telecomunicació de Barcelona

by

Adrián Pérez Portero

In partial fulfillment of the requirements for the Master's degree in
Telecommunications Engineering

supervised by
Prof. Adriano Camps Carmona

and co-supervised by
Mr. Joan Adrià Ruiz de Azúa Ortega
and
Mr. Joan Francesc Muñoz Martín

Barcelona, May 26th, 2019

Abstract

In recent years, Earth Observation (EO) technologies have surged in an attempt to better understand the world we live in, and exploit the vast amount of data that can be collected to improve our lives. The field of EO encompasses a broad array of technologies capable of extracting information remotely, in a process called Remote Sensing (RS). CubeSats are causing a revolution in the RS field, and are becoming a really important contribution to it. The lack of testing and preparation are common in CubeSat EO missions due to the low budgets they usually suffer from. A successful CubeSat EO mission must supply the lack of size or funding with properly tested components and environments. In this document, emphasis will be given to preemptive approaches such as studying the performance of Commercial Off-The-Shelf (COTS) Global Positioning System (GPS) receivers and the development of simulators for highly dynamic environments. This topic will be expanded upon by introducing the problematic of simulating such signals for testing, and the possible countermeasures to Radio-Frequency Interference (RFI) that threatens the success of the mission. Finally, a new S-Band Ground Station will be built to provide access to this band for future CubeSat missions. All of the above will provide a holistic view on some of the hot challenges that EO faces, and multiple future research paths that open with the recent rise of *New Space* technologies.

“May your choices reflect your hopes, not your fears.”
- Nelson Mandela

Acknowledgements

This thesis represents not only the work I have done these last semesters, but the culmination of the time I have spent in this university. And for that, I am thankful to everyone that has been a part of this long journey of learning and self-discovery.

First and foremost, I would like to extend my deepest gratitude to my advisor, Professor Adriano Camps. He allowed me to capitalize on my strengths by providing a stage where I could use them.

I would also like to thank everyone in the NanoSat Lab and different laboratories, especially JuanFran, Lara and Joan Adrià for always entertaining my endless questions and helping me, and Sergi for the great moments we've spent together.

Special thanks to Jorge, who made me feel at home from the very beginning, motivated me to keep trying hard, and provided me with a role model I could follow.

To every single one of my friends, I would like to thank you for always being there, even if life makes it hard to keep in touch.

To my mother, Palmira, and my sisters Monica and Cristina. Their support has been unconditional throughout all these years, and I have nothing but admiration for them.

And last but not least, to Aina, who brightens my days and helps me keep moving forward.

This work is also yours.

List of Figures

2.1	CubeSat Standard sizes	4
2.2	Number of nanosatellites per type. Source: nanosats.eu	4
2.3	Rendered image of the ³ Cat-4	5
2.4	Doppler shift depends on the relative velocity	6
2.5	Observatori Astronòmic del Montsec. Source: jorfe.es	8
3.1	Generic GPS receiver carrier tracking loop block diagram	10
3.2	Third-order PLL with second-order FLL assist	12
3.3	Doppler shift discontinuities	13
4.1	Legacy Navigation message. Source: navipedia.net	15
4.2	GNSS Signal generation iteration	16
4.3	Reference frame for specular point calculation	17
4.4	Specular point and glistening zone mapped to a DDM [1]	18
4.5	DDM calculation process	18
4.6	IQ Data transport for further processing in separate software using sockets.	19
4.7	Early version of the DDM Visualizer	19
4.8	Complete GNSS and GNSS-R Test Bench used in the InLab session during GNSS+R 2019.	20
4.9	u-Center Software showing a lock on the generated GNSS signal	21
4.10	Delay-Doppler Map generated with the GNSS-R Signal Generator	21
5.1	FENIX Hardware, Radio Frequency Stage	26
5.2	FENIX Hardware, Signal Processing Stage	26
5.3	Average SNR degradation for multiple GPS commercial receivers. Chirp with 2 MHz bandwidth and 200 Hz of repetition frequency.	27
5.4	Interference signal at -10 dBm	28

5.5	Comparison of uBlox performance with and without FENIX	28
5.6	Testing the upper limit of FENIX for this combination of GNSS signal plus interference	29
5.7	Interference signal at -30 dBm	29
5.8	Comparison of DDM observables with and without FENIX	30
5.9	New FENIX in a custom-made enclosure manufactured by Balamis S.L.	31
6.1	Satellite Frequency Bands. Source: ESA	32
6.2	Future location of the new S-Band in the Observatori Astronòmic del Montsec (OAdM)	34
6.3	Block diagram of the S-Band Ground Station	35
6.4	Cabling diagram	36
6.5	3m Dish Reflector on top of the Campus Nord D3 building's roof	38
6.6	Maximum Wind Speeds (2y) at the OAdM. Source: iec.cat	38
6.7	Wind Load graph for the 6mm mesh antenna. Source: rfhamdesign.com	39
6.8	UA-02 Heavy Duty bracket plus BIG-RAS/HR	41
6.9	Counter Weight calculation	41
6.10	Block diagram of the software architecture	43
6.11	Hoisting the antenna	44
6.12	Complete assembly at the roof of D3 building	45
6.13	Proposed measurement points for Azimuth Calibration	46
6.14	Intermodulation Products received in Campus Nord (2.2 GHz center, 600 MHz span)	47
6.15	Render of the final installation in the OAdM, next to the already laid foundations	48

List of Tables

3.1	Loop Filter Characteristics	11
3.2	Positioning Errors and TTFF	13
6.1	Transmitter characteristics for the FSSCat mission	34
B.1	Budget of S-band Ground Station	IV

Acronyms

- ADS-B** Automatic Dependent Surveillance—Broadcast. 5
- AIS** Automatic Identification System. 5
- API** Application Programming Interface. 42
- BLAS** Basic Linear Algebra Subprograms. 16
- COCOM** Coordinating Committee for Multilateral Export Controls. 5, 9, 50
- COTS** Commercial Off-The-Shelf. i, 3, 20
- CW** Continuous Wave. 24, 27, 28
- DDM** Delay-Doppler Map. 6, 17–19, 21, 22, 28, 29
- EO** Earth Observation. i, 1, 2, 4, 5, 7–9, 23, 50
- ESA** European Space Agency. 5, 7
- FENIX** Front-End GNSS Interference eXcisor. 7, 14, 20, 25–30, 50, 51
- FLL** Frequency-Locked Loop. 10–12
- FPGA** Field Programmable Gate Array. 17, 26, 29, 30
- GDT** Gas Discharge Tube. 36
- GNSS** Global Navigation Satellite System. 1, 4–7, 9, 10, 12, 14, 20, 22–27, 30, 50, 51
- GNSS-R** GNSS Reflectometry. 1, 5–7, 14, 15, 17, 22, 23, 27, 28, 50

- GPS** Global Positioning System. i, 6, 10, 12, 14, 15, 18, 20, 46
- GR** GNU Radio. 37
- GS** Ground Station. 1, 7, 8, 33, 35, 37, 42, 47–51
- IEEC** Institut d'Estudis Espacials de Catalunya. 33
- INR** Interference-to-Noise Ratio. 28
- IP3** Third-order Intercept Point. 36, 47
- LEO** Low Earth Orbit. 7, 34
- LHCP** Left-Handed Circular Polarization. 37
- LNA** Low-Noise Amplifier. 36, 47
- MFT** Multiresolution Fourier Transform. 24, 25
- MTFF** Mean Time to First Failure. 33
- NF** Noise Figure. 36
- NORAD** North American Aerospace Defense Command. 33
- NP** Neyman-Pearson. 23
- NRE** Non-Recurring Engineering. 3
- OAdM** Observatori Astronòmic del Montsec. v, 8, 33, 34, 36, 38, 40, 42, 47–49
- OC** Operation Center. 42
- P-POD** Poly Picosatellite Orbital Deployer. 3
- PCPS** Parallel Code-Phase Search. 18
- PLL** Phase-Locked Loop. 10–12
- PRN** Pseudo-Random Noise. 6
- RF** Radio Frequency. 6, 25, 26, 35, 36, 47, 49
- RFI** Radio-Frequency Interference. i, 1, 7, 8, 20, 23–30, 46, 47, 50

- RHCP** Right-Handed Circular Polarization. 37
- RO** Radio Occultation. 4, 5, 7, 23
- RS** Remote Sensing. i, 1, 7, 50
- SDR** Software-Defined Radio. 8, 9, 12, 14, 20, 21, 27, 36, 37, 49
- SNR** Signal-to-Noise Ratio. 9, 11, 24, 27
- SP** Signal Processing. 25, 26
- STFT** Short-Time Fourier Transform. 24
- SV** Space Vehicle. 9, 20
- SVG** Scalable Vector Graphics. 19
- TLE** Two-Line Element. 14, 33
- UHF** Ultra High Frequency. 8, 33
- VCO** Voltage-Controlled Oscillator. 9
- VHF** Very High Frequency. 8, 33
- VSWR** Voltage Standing Wave Ratio. 37
- WT** Wavelet Transform. 24

Contents

Abstract	i
Acknowledgements	iii
List of Figures	v
List of Tables	vi
Acronyms	vii
1 Introduction	1
2 State of the Art and Motivation	3
3 Modification of a SDR-based GNSS receiver for high dynamics	9
3.1 High dynamics limitations for commercial GNSS receivers	9
3.2 Tracking in high dynamics	10
4 Implementation of a GPS + GNSS-R signal generator	14
4.1 GPS Signal study	15
4.2 GNSS and GNSS-R simulation	16
4.2.1 Specular point calculation	16
4.2.2 Adding surface scattering	17
4.3 Data processing	17
4.3.1 DDM Calculation	18
4.3.2 DDM Visualization	19
4.4 Testing	20
4.4.1 Simulator testing	20
4.5 Future Work	22

5	GNSS Interference detection and mitigation	23
5.1	Brief theory on Interference detection and mitigation	23
5.2	FENIX	25
5.2.1	Current version	25
5.2.2	FENIX Testing	27
5.2.3	New version	29
6	Design and implementation of an S-band Ground Station at the Observatori Astrònomic del Montsec	32
6.1	Basic principles of a Ground Station	33
6.2	Design and Link Budget	33
6.2.1	RF Chain	35
6.2.2	Antenna	37
6.2.3	Rotor	40
6.2.4	Software	42
6.3	Testing	42
6.3.1	Assembly	42
6.3.2	Calibration	44
6.3.3	Interferences	46
6.4	Installation in the OAdM	47
6.5	Conclusions and Future Work	48
7	Conclusion and Future Research	50
Bibliography		52
Appendix A S-Band Downlink Link Budget		I
Appendix B Budget		III

CHAPTER 1

Introduction

In recent years, many Earth Observation (EO) technologies have been developed in an attempt to better understand the world we live in, and exploit the vast amount of data that can be collected to improve our lives. The field of EO encompasses a broad range of technologies capable of extracting information remotely, in a process called Remote Sensing (RS).

In this document, several technologies related to RS are studied with the objective to obtain holistic knowledge of such systems. First of all, an overview of the current state of EO is discussed, while introducing CubeSats as a new and important player in this field. CubeSats entail not only low cost and rapid iteration, but new and interesting problems such as miniaturization of technology and severe power constraints.

These downsides will be expanded upon, while also focusing on the quirks that allow for CubeSats to thrive alongside big spacecraft missions in different space agencies. The lack of testing and preparation are common in CubeSat EO missions due to the low budgets they usually suffer from. This work will focus heavily on the ground segment of Global Navigation Satellite System (GNSS)-related technologies, which are used in the Remote Sensing Lab and the NanoSat Lab in UPC for EO. As part of these technologies, several improvements in system knowledge and simulation are explored. In parallel, a more and more relevant Radio-Frequency Interference (RFI)-mitigation technology is introduced by capitalizing on the new simulation solutions. Both its effects on commercial GNSS receivers and GNSS Reflectometry (GNSS-R) systems are examined.

Finally, a new Ground Station (GS) has been designed and built for the newest UPC CubeSat missions requiring S-band downlinks.

This research will show the importance of the ground segment of any EO mission, as simulations, testing and proper equipment are key to a successful campaign.

CHAPTER 2

State of the Art and Motivation

In the long quest to understand the universe we live in, humans have strived to engineer ways to observe the environment and extract as much information as possible. In recent years, a large amount of this data is obtained from satellites orbiting the Earth, performing Remote Sensing by processing the signals that are emitted or reflected from it. At the beginning of the space age, all satellites were "small", such as Sputnik-1 or Explorer-1. There was no standardization of the size or shape of the satellites, and each had its own design. It was not until the end of the 70s that standard spacecraft buses appeared, prompted by a need of reducing Non-Recurring Engineering (NRE). In the early 80s, micro-satellites emerged and used Commercial Off-The-Shelf (COTS) components to try and reduce costs. This paradigm shift continued by focusing on simpler satellites with tighter budgets and single mission objectives, maximizing the scientific return per money spent.

The CubeSat standard [2] was created by Profs. J. Puig-Suari (California Polytechnic State University), and Bob Twiggs (Stanford University's Space Systems Development Lab) in 1999 to reduce development time and cost, and to facilitate access to space to university students. CubeSats were defined as cube shaped picosatellites with a length of 100 mm per side and 1 kg of mass. This configuration is called a 1U (unit) CubeSat. Current CubeSat Design Specification defines the envelopes for 1U, 1.5U, 2U, 3U, and 3U+, and 6U form factors, and work in progress for 12U and PocketQubes as seen in Figure 2.1.

It facilitates frequent and affordable access to space with launch opportunities available on most launch vehicles by standardizing a size and launch method (Poly Picosatellite Orbital Deployer (P-POD)).

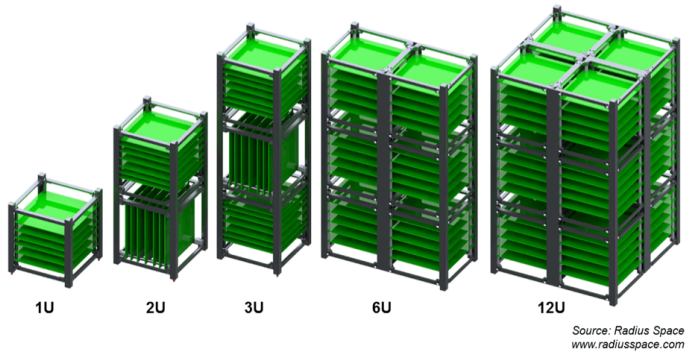


Figure 2.1: CubeSat Standard sizes

Today, 3U CubeSats are dominating the scene (Figure 2.2), and predictions say they will over the next decade. They possess the right balance between very capable payloads and limited manufacturing and launch costs.

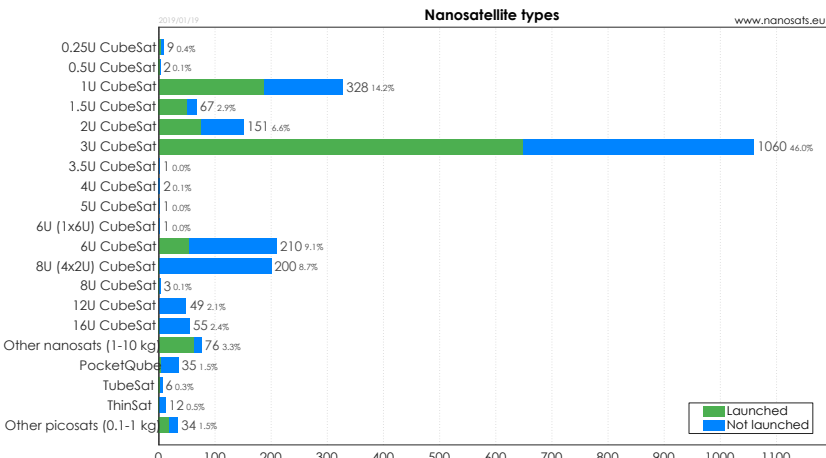


Figure 2.2: Number of nanosatellites per type. Source: nanosats.eu

On the subject of payloads, the most prevalent use cases are Earth Science, Astrophysics and Biological and Physical Sciences. Optical EO, where satellites take pictures at different wavelengths to obtain information, is the main application of nanosatellites, followed by GNSS-Radio Occultation (RO) and telecommunication services. With the rapid investment and advancements in payload development, such as deployable solar panels and improved downlinks, multitude of science missions that were considered unfeasible for CubeSats have recently been proven to be possible.

Even though Optical EO is of great interest due to the current advance-

ments in Deep Learning that can make use of the vast amounts of data generated, this work studied Passive Microwave EO and GNSS-R missions due to power and bandwidth limitations usually found in CubeSat systems.

This approach is shared by many new start-ups in the EO industry. One such example is Spire [3], a company that uses large amounts of CubeSats to get rapidly refreshed information on the planet. While traditional EO missions have always been big and costly, their data output is usually limited, with low coverage of the Earth's surface at a given time, and discontinued when the mission ends. Spire aims at maintaining a persistent view of 97% of Earth by having a 120 CubeSat network with short lifespan so that they can follow the development pace of technology. Spire mainly carries GNSS-RO payloads, with Automatic Identification System (AIS) and Automatic Dependent Surveillance—Broadcast (ADS-B) as added services, and soon will start boarding GNSS-R payloads as well.

The ³Cat-4 [4] mission (Figure 2.3), created at the NanoSat Lab UPC and backed by the European Space Agency (ESA) Fly your Satellite [5] programme, has a similar payload as the one found in Spire.

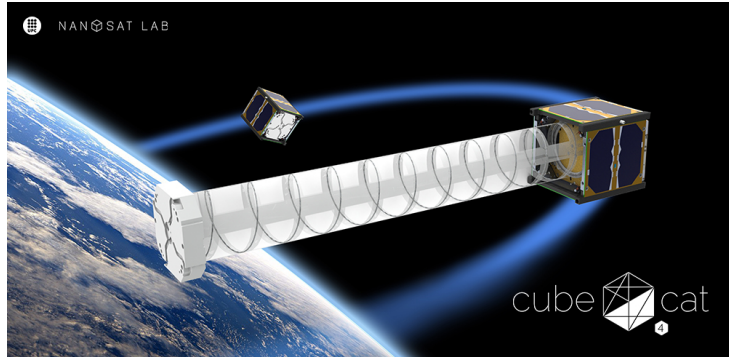


Figure 2.3: Rendered image of the ³Cat-4

For missions like ³Cat-4 or Spire, which depend on GNSS signals to correctly harvest data through techniques such as GNSS-R, GNSS reception is crucial for being able to accurately track its position, thus allowing for a correct mapping between the harvested data and the coordinates it was taken in. Usually, there are several problems with GNSS reception, both in high dynamics and normal conditions.

The first one is that GNSS receivers are constrained by what is called the Coordinating Committee for Multilateral Export Controls (COCOM) limits, by the US government, that disable solving the GPS signals for positioning above a certain height and speed. It is possible to purchase receivers with the limits disabled with permission from the US government, but that is

not the only problem that GNSS reception in high dynamics environments such as the ones found in satellite receivers face. At such speeds, the signal transmitted from the satellite suffers from Doppler shifts, as seen in Figure 2.4, and it can be hard to track due to the rapid variation of the Doppler shift due to the relative velocity between the transmitting satellite and the receiver.

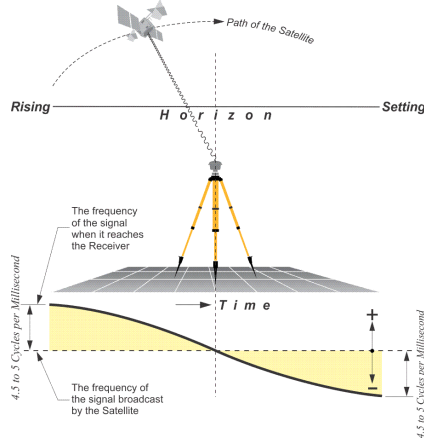


Figure 2.4: Doppler shift depends on the relative velocity

In the field of adaptive filtering and tracking of Radio Frequency (RF) signals, it is common to use open and closed loops to compensate for these frequency shifts. There is a basic trade-off that is hard to circumvent: the larger the bandwidth of the loop filter is given so as to rapidly track changes in the carrier signal frequency, the more noise is introduced in the system. The opposite is also true: the narrower the filter, the least amount of noise is introduced, but also the more likely the system is to lose lock on the carrier signal when it leaves the filter bandwidth. This tradeoff will be studied in Chapter 3 by means of implementing a software-defined GNSS receiver capable of correctly tracking doppler shifts in high dynamics environments.

Delay-Doppler Maps (DDMs) contain all the information in GNSS-R receivers. In conventional GNSS-R (cGNSS-R), they are generated by correlating the GNSS signal after reflecting off Earth by a search space consisting of the Pseudo-Random Noise (PRN) code of a Global Positioning System (GPS) satellite shifted in both Delay and Doppler [6]. It is then interesting before launching such a payload, to test the equipment with signals such as the ones that will be received (both directly and after reflection on Earth). The cost of a high-dynamics GNSS simulator such as the one from Spirent is too high and prohibitive for companies or universities deploying CubeSats, forcing them to launch non-tested technology, which then may cause a failure

or malfunction on the entire spacecraft. Thus, a complete GNSS / GNSS-R simulator was implemented to allow for testing in such an environment. This work was first showcased publicly in the 2019 IEEE GNSS+R Workshop [7], under the title "Implementation of a testbed for GNSS-R payload performance evaluation". The main premise of this software will be presented in Chapter 4.

Another problem that usually hinders the performance of GNSS receivers is RFI. RFI signals are a current threat for GNSS receivers due to their very low power signals. Due to the difference in power, the samples get totally corrupted by RFI and recovering the original GNSS signal becomes impossible. Regulations to protect reserved frequency bands are not enough to solve the problem of RFI. Unintentional RFI is defined as RFI that is not produced to deliberately harm third party systems. Examples of such RFI are lower harmonics, inter-modulation products, bands overlapping, out-of-band emissions, etc. There is also the threat of Intentional RFI. Nowadays, it is very cheap and easy to create signal jammers for any frequency. A recent discovery even revealed a 3\$ GPS spoofer created with an USB to VGA dongle [8].

It is then critical to provide any system that is reliant on GNSS signals with interference detection and mitigation techniques [9, 10]. Chapter 5 will describe the Front-End GNSS Interference eXcisor (FENIX), an RFI detector and mitigator developed in UPC [11]. It was created due to the proliferation of RFI, as it has become one of the most concerning topics in microwave radiometry and GNSS-based devices not only for navigation, positioning and timing, but also for EO purposes, such as GNSS-R and RO due to the corruption of the received signal and the corresponding geophysical measurements. The technologies that enable it and the future plans for this device will be explored, as well as the performance tests in conjunction with the GNSS signal generator.

Finally, once some of the most important techniques for ensuring the success of a RS mission are met, it is of utmost importance to be capable of downloading the scientific yield of the payloads in the satellite. A GS is a complex ground equipment that has historically been exclusive to space agencies such as ESA, NASA, Roscosmos and JAXA. Tracking satellites with enough precision, and being capable of amplifying the signals enough to reach space is a difficult endeavor. Some companies such as Amazon now even offer GSs as a service [12] to any customer, allowing to schedule passes and download data. This service hints at the difficulties of maintaining GSs, as for an institution capable of launching satellites to be unable to create their own network of GSs and having to resort to renting them is proof enough. Luckily, in the recent years, the proliferation of Low Earth Orbit (LEO) satellites



Figure 2.5: Observatori Astronòmic del Montsec. Source: jorfe.es

with their shorter distances than at other orbits and Software-Defined Radio (SDR) making it cheap to create custom receivers have made it achievable for institutions such as the NanoSat Lab to build and operate their own GSs. As radio wave frequencies increase, they gain more bandwidth at the sacrifice of transmission distance. The amount of RFI found at the lower frequency bands (Ultra High Frequency (UHF) / Very High Frequency (VHF)), together with the prospects of wider bandwidths, have resulted in an almost total shift of EO missions to higher bands such as S-band. As a consequence of this, both in order to maintain compatibility with other missions and to take advantage of the higher data rates, a new S-Band GS will be built for the NanoSat Laboratory. This report will detail in Chapter 6 the conception, design, implementation and operation of the new S-band GS located in the Observatori Astronòmic del Montsec (OAdM) (Figure 2.5), prompted by the soon-to-be launched FSSCat [13] mission, which will use S-band frequencies instead of UHF / VHF like previous UPC NanoSat Lab missions.

CHAPTER 3

Modification of a SDR-based GNSS receiver for high dynamics

In orbit, EO Satellites that must receive GNSS signals face the problems associated to high dynamic environments such as a high Doppler rate, which makes tracking the signal a difficult task. The larger the relative velocity between Space Vehicles (SVs), the larger the observed Doppler shift, up to a maximum of ± 45 kHz [14] as satellite velocity increases with lower altitude. Traditionally, loop filters are used to reduce noise and produce an accurate estimate of the original signal at its output. The loop filter order and noise bandwidth also determine the its response to signal dynamics [15]. By using a wider bandwidth, filters are able to track signals with high Doppler rates, at the cost of introducing more noise into the system. This noise can then affect the reception at low Signal-to-Noise Ratio (SNR), and cause lower precision when used for positioning.

3.1 High dynamics limitations for commercial GNSS receivers

GNSS receivers are usually restricted in a way that only devices moving slower than 1,900 km/h and at an altitude lower than 18,000 m are able to obtain a position fix. These are called the COCOM limits, and are enforced by the U.S. Department of Commerce. This work aims at continuing the algorithm research, development and implementation of GNSS receiver for high dynamic conditions based on low-cost SDRs.

The discriminator, which controls the Voltage-Controlled Oscillator (VCO)

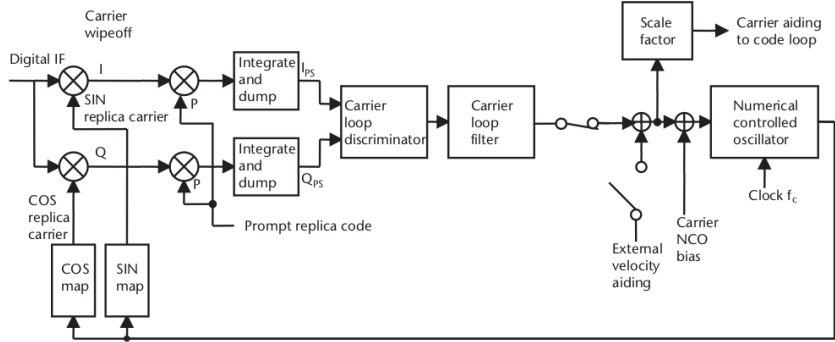


Figure 3.1: Generic GPS receiver carrier tracking loop block diagram

for each loop iteration, defines the type of tracking loop as a Phase-Locked Loop (PLL) or a Frequency-Locked Loop (FLL). As the PLL minimizes the difference between the phases of two periodic waveforms, the FLL minimizes the difference in frequency. However, given the fact that the derivative of the phase is the frequency, phase locking guarantees frequency locking. On the contrary, two signals that are frequency locked will have an uncontrolled relative phase, and may even drift over time. Thus, tracking phase is more accurate than tracking frequency, but it is more sensitive to dynamic stress due to the fact that it is slower to eventually track frequency by continuously tracking phase.

3.2 Tracking in high dynamics

In order to receive the modulated data from GNSS signals, the receiver has to constantly track the carrier frequency through Doppler shifts. Figure 3.1 presents a block diagram of a GPS receiver carrier tracking loop. In order to characterize the loop, focus is needed on its three most important blocks: the predetection integrators, the discriminators and the filters. They determine the carrier loop thermal noise error and the maximum dynamic stress threshold.

The predetection integrator defines the amount of time the incoming signal is integrated before proceeding. The smaller this time, the more likely it is that the loop will follow a change in the signal due to the faster update time. The filter defines the bandwidth of the loop so that it will try to lock onto signals in-band. Finally, the discriminator defines the type of tracking loop as a PLL or a FLL by producing a phase or frequency error estimate depending on the incoming signal.

To tolerate dynamic stress, the predetection integration time should be

short, the discriminator should be an FLL, and the carrier loop filter bandwidth should be wide. However, for the carrier measurements to be accurate (have low noise), the predetection integration time should be long, the discriminator should be a PLL, and the carrier loop filter noise bandwidth should be narrow.

Table 3.1: Loop Filter Characteristics

Loop Order	Noise Bandwidth B_n (Hz)	Typical Filter Values	Steady State Error
1st	$\frac{\omega_0}{4}$	ω_0 $B_n = 0.25\omega_0$	$\frac{dR/dt}{\omega_0}$
2nd	$\frac{\omega_0(1 + a_2^2)}{4a_2}$	ω_0^2 $a_2\omega_0 = 1.414\omega_0$ $B_n = 0.53\omega_0$	$\frac{d^2R/dt^2}{\omega_0^2}$
3rd	$\frac{\omega_0(a_3b_3^2 + a_3^2 - b_3)}{4(a_3b_3 - 1)}$	ω_0^3 $a_3\omega_0^2 = 1.1\omega_0^2$ $b_3\omega_0 = 2.4\omega_0$ $B_n = 0.7845\omega_0$	$\frac{d^3R/dt^3}{\omega_0^3}$

The standard PLL-based architectures are somehow limited because of the noise reduction vs. dynamic range compromise, which may lead the filters to lose lock. This tradeoff is mainly driven by the bandwidth and order of the loop. A small bandwidth is needed to filter out as much noise as possible to be able to operate at low SNR, whereas a large one is required for coping with fast variations of the parameters of interest.

The loop's order also plays an important role in such scenarios, as seen in Table 3.1. For instance, the 2nd order PLL is unconditionally stable at all noise bandwidths, but it is not suitable to deal with complex dynamics such as those caused by the acceleration of the satellite. The 3rd order PLL, while being more flexible in front of high dynamics, only remains stable for bandwidths below 18 Hz [16]. It is also important to take into account that the PLL has a constant bandwidth, a priori fixed by the designer.

The FLL-Aided PLL architecture aims to solve the tradeoff by using both filters at different stages of signal lock [17]. As seen in Figure 3.2, if the PLL error input is zeroed in either of these filters, the filter becomes a pure FLL. Similarly, if the FLL error input is zeroed, the filter becomes a pure PLL.

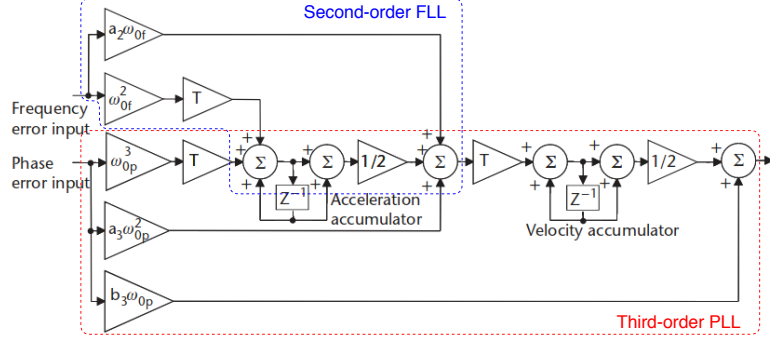


Figure 3.2: Third-order PLL with second-order FLL assist

The lowest noise loop closure process is to close in pure FLL, then apply the error inputs from both discriminators as an FLL-assisted PLL until phase lock is achieved, then convert to pure PLL until phase lock is lost.

If the noise bandwidth parameters are chosen correctly, there is very little loss in the ideal carrier tracking threshold performance when both discriminators are continuously operated.

In order to characterize this architecture, a test bench was created using GNSS-SDR [18], an open source software receiver for GNSS, a DVB-T dongle based on the Realtek RTL2832U [19] that can be used as an SDR receiver and a R&S SMU200A Vector Signal Generator [20] to simulate the GNSS signals received in a high dynamics environment.

The results (Table 3.2) were mostly satisfactory, but the carrier tracking loop lost lock at fixed intervals, hinting at a systematic problem. After evaluating the carrier frequencies generated by the SMU200A, it is easy to see that the interpolation done by the equipment to generate intermediate frequency steps in between satellite waypoints was not precise enough.

In Figure 3.3, the discontinuities appeared every second, which coincidentally is also the update rate of the waypoints introduced to generate the orbit. Due to this, one had to increase the filter bandwidth far too much in order to track these artificially-created doppler shifts to generate coherent results. On the contrary, the SMU200A did not allow for a more fine-grained waypoint definition, thus becoming useless for this kind of precise testing. This became a motivation to create an in-house GPS signal generator, as will be seen in Chapter 4. Other, more robust, solutions such as the use of Kalman filters has yet to be studied using the new GPS signal generator.

Table 3.2: Positioning Errors and TTFF

PLL_{BW} (Hz)	FLL_{BW} (Hz)	TTFF (s)	RMS Vertical (m)	RMS Horizontal (m)	RMS Error (m)
60	7	199	80,40	0,003	80,40
	14	143	4,88	0,003	4,88
70	7	148,6	20,76	0,004	20,76
	14	150	166,69	0,45	166,69
80	7	143	4,92	0,004	4,92
	14	197	18,47	0,003	18,47
90	7	143	4,92	0,004	4,92
	14	145,8	5,17	0,003	5,17
100	7	143	4,92	0,004	4,92
	14	143	4,93	0,004	4,93

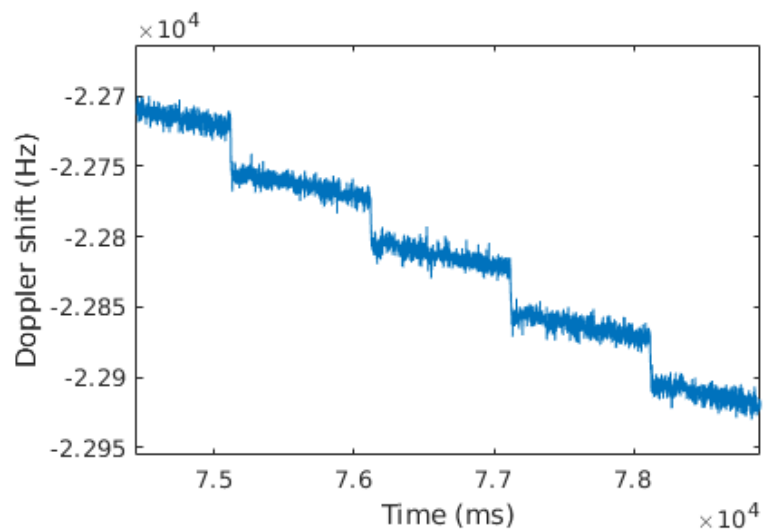


Figure 3.3: Doppler shift discontinuities

CHAPTER 4

Implementation of a GPS + GNSS-R signal generator

In space applications, the validation of any in-flight instruments is critical to prepare for unforeseen events. High-dynamics GNSS receivers based on SDR, GNSS-R payloads based on SDR are under deployment by several institutions, but conversely are hard to test. The cost of a High-dynamics GNSS simulator such as the ones manufactured by Spirent [21] is prohibitive for companies or universities deploying CubeSats, forcing them to launch non-tested technology, which then may cause a failure or malfunction on the entire spacecraft. Even commercial simulators such as the R&S SMU200A [20] may be insufficient for applications that require precision such as the ones discussed in Chapter 3, causing systematic errors that could have lead to inadequate configurations (oversized bandwidths).

As a means of being capable of testing hardware at the NanoSat Laboratory, the creation of a GPS Direct + Reflected signal simulator began. In order to test both FENIX and GNSS-R equipment, a series of requirements were set:

- For GPS receivers to achieve a lock on the signal, valid Ephemeris and NAV messages have to be transmitted.
- Any user-defined path can be loaded, be it on Earth or in Space, and with as much temporal resolution as wanted. Two-Line Elements (TLEs) can also be used as a source.
- It should be capable of generating Direct and Reflected paths both on rough and flat surfaces.

- In the case of GNSS-R, a visualizer should also be developed to test the software.

4.1 GPS Signal study

GPS satellites transmit right-hand circularly polarized signals to the earth at two frequencies, designated L1 and L2. The main GPS carrier signal L1, at 1575.42 MHz, is modulated by two codes: the coarse/acquisition (C/A) code also known as civilian code and the precision/secure (P/Y) code, reserved by cryptographic techniques to military and authorized civilian users.

The Navigation Message provides all the necessary information to allow the user to perform the positioning service. It includes the Ephemeris parameters, that define a Keplerian orbit and are needed to compute the satellite coordinates with enough accuracy, the Time parameters and Clock Corrections, to compute satellite clock offsets and time conversions, the Service Parameters with satellite health information (used to identify the navigation data set), Ionospheric parameters model needed for single frequency receivers, and the Almanacs, allowing the computation of the position of all satellites in the constellation, with a reduced accuracy (1 - 2 km of $1-\sigma$ error), which is needed for the acquisition of the signal by the receiver. The ephemeris and clocks parameters are usually updated every two hours, while the almanac is updated at least every six days.

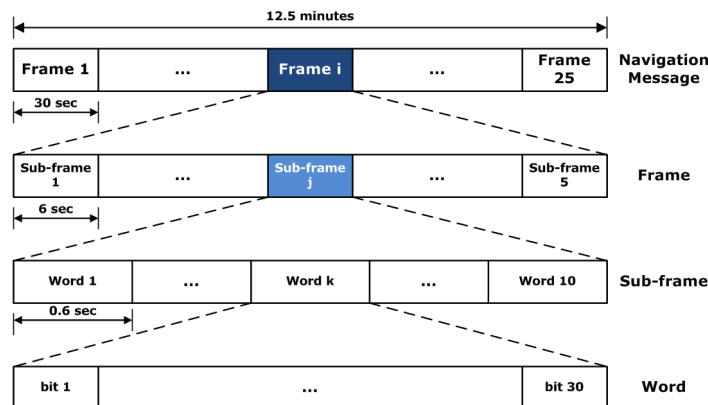


Figure 4.1: Legacy Navigation message. Source: navipedia.net

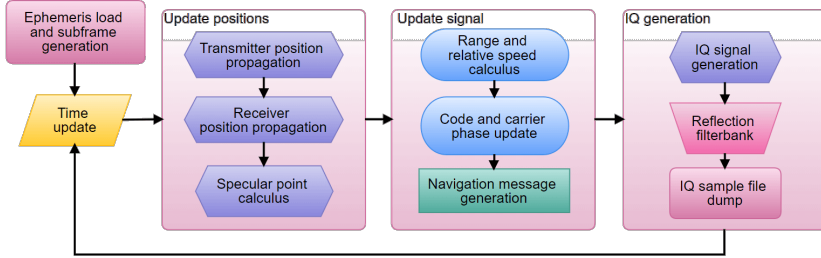


Figure 4.2: GNSS Signal generation iteration

4.2 GNSS and GNSS-R simulation

For our use case, the main parameters we have to add are the Ephemeris parameters, and the Almanac. In Figure 4.2, the main loop for the generation of the signal can be seen. For each position of the receiver, and each delta of time, the navigation message, subframes, paths and distances are recalculated, thus generating the waveform to be transmitted. In Figure 4.1, the entire NAV message can be seen. Conversely to the SMU200A discussed in Chapter 3, this simulator is capable of generating a signal with a time step as small as desired, making it capable of more realistically simulating the Doppler shift and other physical properties of the signal at the cost of a higher computational load.

In the case of the reflected signal, several other steps have to be taken to calculate the waveform.

4.2.1 Specular point calculation

First of all, the Specular Point of the reflection of the signal on the Earth's surface must be precisely calculated. In order to do that, the algorithm by Gleason et al. [22] is used. The original script, coded in Matlab and no longer found on his website, was converted to C and upgraded with the use of Basic Linear Algebra Subprograms (BLAS) to accelerate it.

To calculate the Specular Point implies creating a new reference frame, as shown in Figure 4.3, that includes the WGS84 Earth [23] and the transmitting and receiving satellites. The specular point will be located at the location on the surface of the WGS84 ellipsoid where both incident angles from the rays traced between each satellite and the same point are equal. An iterative approach is used to find this point, until the difference between angles is negligible. With this new point, the new path for the signal to traverse is created, and it is used to calculate the new phase and delay.

4.2.2 Adding surface scattering

However, the previous calculation will only generate a specular reflection on the GNSS-R receiver. Over rough surfaces such as the sea affected by wind or land, surface scattering occurs around the specular reflection, and interesting parameters can be extracted from this signal. For example, as seen in Zavorotny and Voronovich [24], the wind speed can be extracted for the delay and Doppler spread. In order to properly simulate the glistening zone, as seen in Figure 4.4, several other factors have to be taken into account. As per Zavorotny and Voronovich [24], the relationship between the original signal and the scattered signal can be understood as a series of shifts in frequency and delay. Each shift is then scaled according to the area corresponding with each delay and doppler pair, as seen in Figure 4.4. This scaling can be better understood through the work in Marchan-Hernandez et al. [25], where a Jacobian matrix can be used to scale each value in the DDM to create the characteristic horseshoe of scattered reflections.

All of the previous calculations do not yet take into account the randomness of the reflections, with which the tails of the horseshoe should have less power than the head. Ionospheric effects such as delay are not factored in either. Even with these limitations, the software is not capable of running in real time: it currently generates about 1 second of data in 10 seconds.

4.3 Data processing

The NanoSat Lab Team developed a DDM calculator for the FSSCat mission. This software, designed to run in an Field Programmable Gate Array (FPGA) inside the satellite, had to be modified to test the signal generator on the ground.

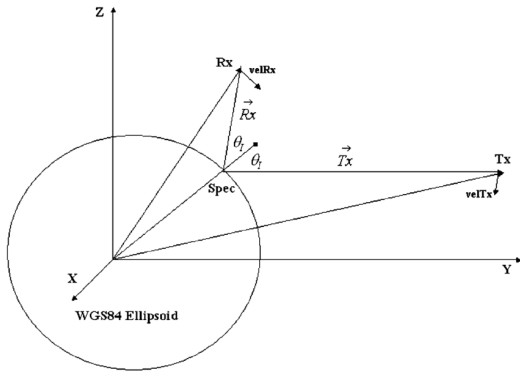


Figure 4.3: Reference frame for specular point calculation

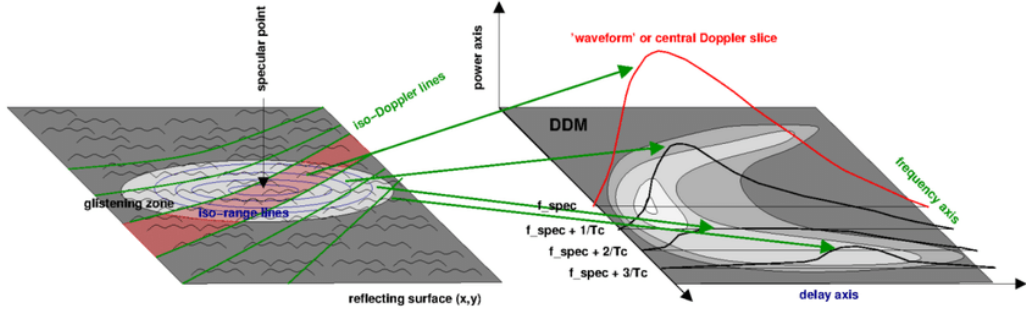


Figure 4.4: Specular point and glistening zone mapped to a DDM [1]

In order to optimize the visualization of the DDM and to accelerate the development cycle, both a DDM calculator and a DDM visualizer were developed.

4.3.1 DDM Calculation

In order to compute a DDM, first of all signal acquisition has to be performed. The optimal solution for current CPUs is to perform what is called Parallel Code-Phase Search (PCPS) [16]. In order to synchronize our receiver to the transmitted GPS signal, it has to acquire the current Doppler frequency as well as the current chip delay. In PCPS, all possible code-replica FFT Doppler shifts (161 bins in this case) are pre-computed and stored in RAM in steps of 500 Hz (40 kHz of span [14]). The FFT of the incoming signal is then multiplied by a reduced set of the pre-computed replicas (i.e. 80 bins), and then the IFFT is calculated. The result from the convolution is module squared and accumulated (incoherent averaging). This process can be seen in Figure 4.5.

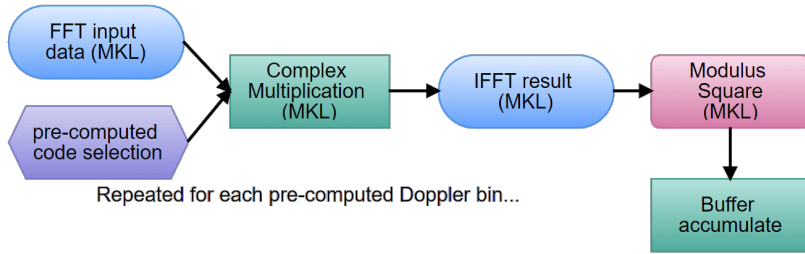


Figure 4.5: DDM calculation process

The result is a heatmap for each delay and Doppler bin of the signal

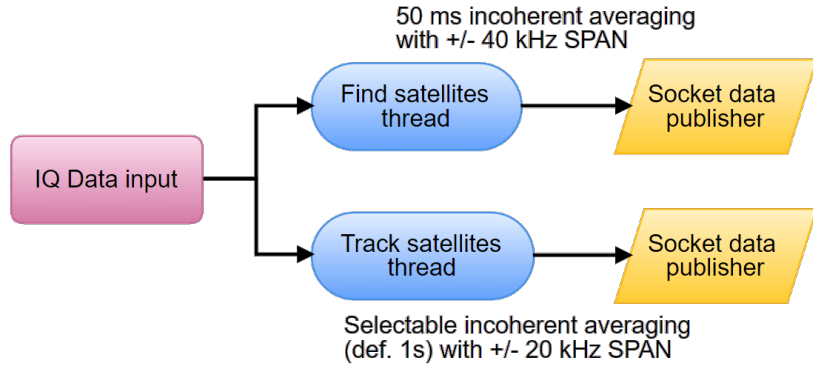


Figure 4.6: IQ Data transport for further processing in separate software using sockets.

power that has to be plotted in a color scale. This is the main objective of the DDM visualizer.

4.3.2 DDM Visualization

In order to visualize the data in real time, and also to be able to share the results remotely, a website in Node.js was programmed.

The DDM Calculation software was designed with a modular approach. Thanks to this, the output of the final heatmap was converted into a JSON array and sent to a remote web server (Figure 4.6), where a specialized software converted it into a Scalable Vector Graphics (SVG) image embedded in a website in real time (Figure 4.7). Thus, anyone who visited this website could view the DDMs in real time.

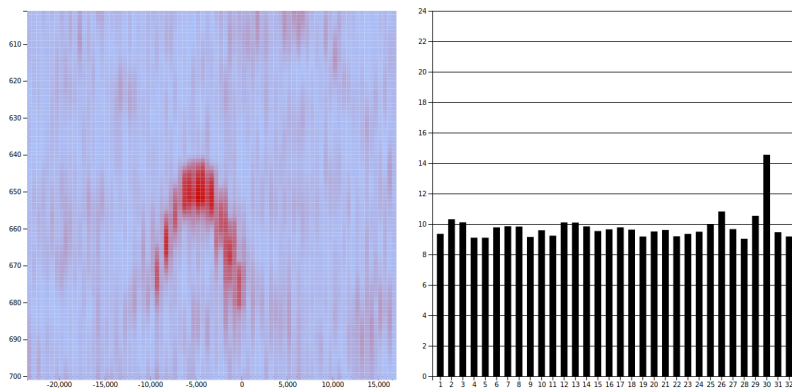


Figure 4.7: Early version of the DDM Visualizer

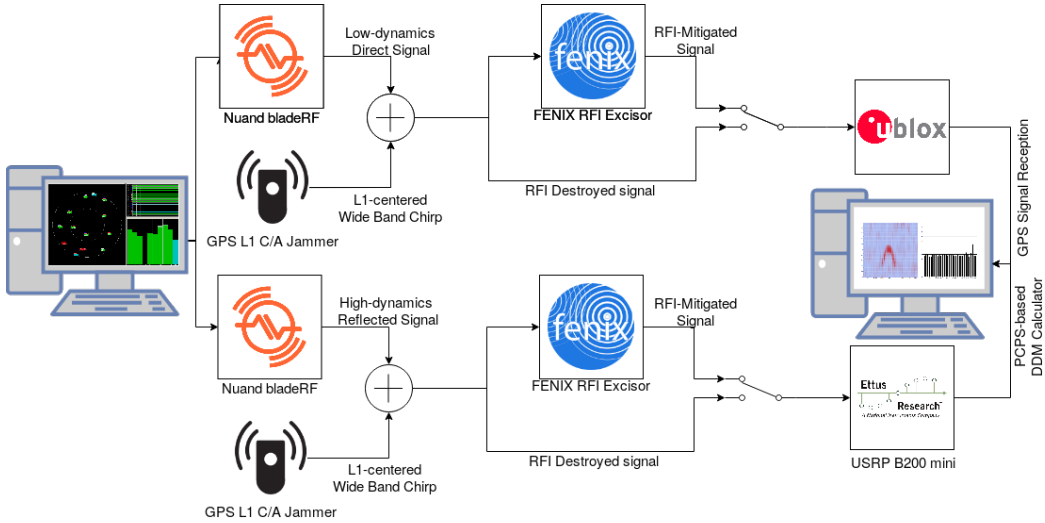


Figure 4.8: Complete GNSS and GNSS-R Test Bench used in the InLab session during GNSS+R 2019.

4.4 Testing

The testbench described in Figure 4.8 was presented in the 2019 IEEE GNSS+R Workshop, to demonstrate both the Signal Generator in conjunction with the FENIX system, that will be introduced in Chapter 5. In order to showcase the simulator, a simple testbed was prepared with two separate paths for the direct and reflected signal. The effects of jamming and RFI Mitigation techniques (FENIX) will be explored in both cases in the next Chapter.

4.4.1 Simulator testing

The first test was to generate a direct GPS signal that could be acquired and tracked by a COTS GPS receiver. The signal was generated with the Simulator, and then streamed using a bladeRF [26] SDR connected directly to a uBlox [27] GPS receiver.

The receiver was able to acquire lock as seen in Figure 4.9, displayed the same SV that were generated by software and the position resolved to Japan, where we had placed our test GNSS receiver. The GPS clock can be set at any point in time (past, present or even future if the Ephemeris for that day are released), but for this demonstration, we used a date 2 weeks in the past. The elevation mask was also shown to work, as the only SV that appeared were those with specular reflections up to -20° of elevation of the satellite's

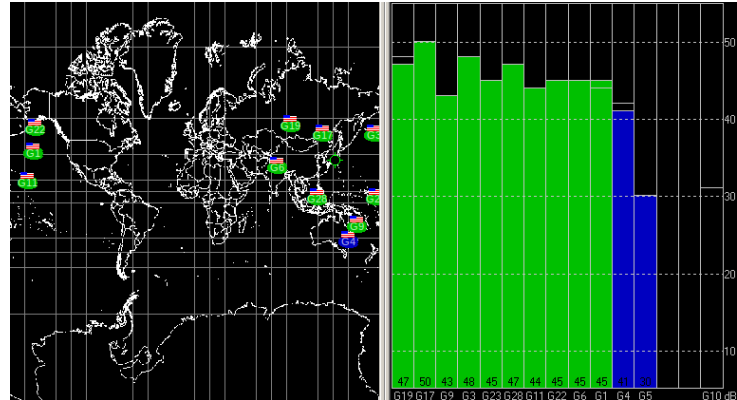


Figure 4.9: u-Center Software showing a lock on the generated GNSS signal

down-looking antenna.

The second test was to generate a reflected signal over sea surface, and receive it with the DDM calculator, displaying the results in a website for everyone to see.

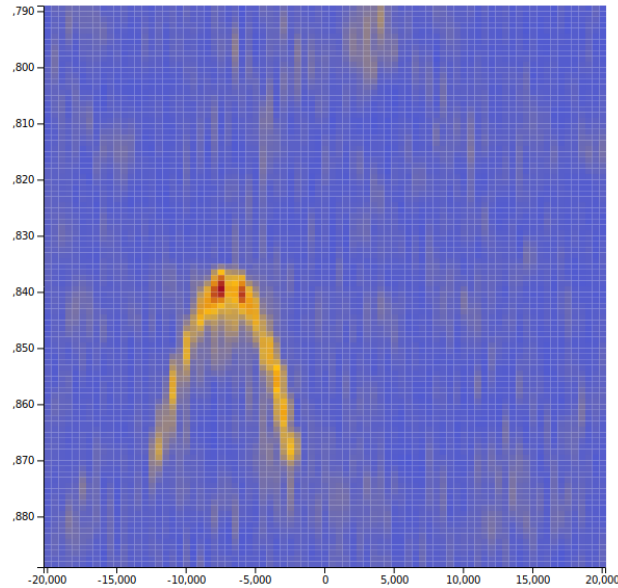


Figure 4.10: Delay-Doppler Map generated with the GNSS-R Signal Generator

The reflected signal (high dynamics) was streamed from a second bladeRF SDR towards a USRP B205mini SDR acting as a receiver (which could be any moving on static vehicle, even spaceborne). The signal was cross-correlated

to produce a DDM, and shown both on screen and on any browser through the DDM Visualizer using a QR-Code with the link. Figure 4.10 shows the result.

4.5 Future Work

To accurately model GNSS and GNSS-R signals requires for multitude of models to be implemented. One example of such models is that of the Ionosphere (Ionospheric delays and scintillations). Other models such as the effects of random components depending on wave heights or transitions from rough to specular surfaces are planned to be added too.

Extensive optimization to achieve real-time operation and more GNSS systems are also being implemented.

CHAPTER 5

GNSS Interference detection and mitigation

The number of applications based on GNSS has been increasing in the last years. With its proliferation, RFI has become one of the most concerning topics on GNSS-based devices, not only for navigation, positioning and timing, but also for EO purposes such as GNSS-R and RO due to the corruption of the received signal and the corresponding geophysical measurements. In this section, a proposed solution to RFI in both GNSS and GNSS-R applications will be explored and later tested with the software developed in Chapter 4.

5.1 Brief theory on Interference detection and mitigation

The problem of mitigating RFI involves the detection of stochastic signals with usually unknown parameters. For this reason, the RFI detection criterion should be based on the Neyman-Pearson (NP) hypothesis testing where a threshold value α is defined to discriminate between RFI-contaminated samples (H_1 hypothesis) and RFI-clean samples (H_0 hypothesis) [28]. Defining the probability to detect RFIs as P_D and the probability to eliminate RFI-clean data falsely as P_{FA} , the NP lemma allows us to obtain a decision threshold to achieve a fixed P_{FA} based on the statistics of both hypotheses (H_0 and H_1). The threshold value α is:

$$\alpha = P(\Lambda(X) \leq \eta \mid H_0), \quad (5.1)$$

where η is the threshold for the likelihood-ratio test,

$$\Lambda(x) := \frac{\mathcal{L}(\theta_0 | x)}{\mathcal{L}(\theta_1 | x)} \quad (5.2)$$

and $\mathcal{L}(\theta | x)$ is the likelihood function. Then, the lemma states that $\Lambda(x)$ is the most powerful test at significance level α .

For GNSS applications, H_0 will always have a Gaussian distribution, as the SNR is usually below 0. However, the undetermined parameters of the RFIs make estimating the distribution of H_1 very difficult.

Several pre-correlation techniques exist in different domains that are strong against certain types of RFI:

- **Time domain techniques:** One of the simplest techniques that consist in sampling the received signal and comparing its power with a threshold α directly related to the power of the signal in H_0 . This kind of excision is adequate for strong and short bursts of RFI, whereas weak and long-lasting RFI may pass undetected. Some examples of this techniques are Pulse Blanking and Amplitude Domain Processing.
- **Frequency domain techniques:** The non-parametric methods consist on comparing the spectrum of the received signal with a theoretical threshold α . These techniques have the same effect as a notch filter. This approach is not useful for non-stationary interference removal, as signals can change quickly in time. Notch Filtering and Frequency Blanking are the most used.
- **Time-Frequency space techniques:** They are the most used for detection and mitigation of RFI. These techniques take into account the fact that RFI spans both the time and frequency domain, thus being able to detect Continuous Wave (CW) and pulsed signals simultaneously. Since GPS signals are low power and wideband signals, the high power jammer signals can usually be distinguished very easily in time-frequency space. Some examples include Spectrogram Blanking and Filter Banks.

Usually, RFI signals have their power concentrated in either time, frequency, or both domain, in order to maximize the instantaneous and/or spectral power density. The Multiresolution Fourier Transform (MFT) directly combines the Short-Time Fourier Transform (STFT) and the Wavelet Transform (WT) to give a representation in three dimensions, a mathematical space defined by the domains of time, frequency, and scale, with different

ratios of time-frequency resolution. It is then more probable to be able to detect the RFI signal within these domains, and subsequently mitigating it.

Statistical tests, typically normality tests such as Kurtosis, are used to determine if a set of samples belongs to a certain statistical distribution or not. Kurtosis is a measure of the "tailedness" of the probability distribution of a random variable. This means that a higher kurtosis is the result of infrequent extreme deviations (or outliers), as opposed to frequent modestly sized deviations. Kurtosis is defined as:

$$\text{Kurt}[X] = E \left[\left(\frac{X-\mu}{\sigma} \right)^4 \right] = \frac{\mu_4}{\sigma^4} = \frac{E[(X-\mu)^4]}{(E[(X-\mu)^2])^2}, \quad (5.3)$$

where μ_4 is the fourth central moment and σ is the standard deviation. Excess kurtosis is defined as the value of the kurtosis minus 3. For a real-valued random variable with a Gaussian (Normal) distribution, excess kurtosis is 0, meaning that the Kurtosis for a Gaussian-shaped signal such as GNSS signals should be 3. Variations from this value indicate the presence of RFI.

The input signal, which is the aggregated of the GNSS signal and the possible RFI signal, is linearly transformed using a given basis. Its main purpose is that the energy of the RFI signal gets concentrated in the smallest possible number of bins in the transformed domain, and hence, it is more easily detected. Then, if it does not belong to the expected statistical distribution (i.e. Kurtosis over and under certain thresholds), the bin is discarded.

5.2 FENIX

FENIX represents the main contribution in the PhD thesis of Dr. Querol Borràs [11]. As its name states, the Front-End GNSS Interference eXcisor (FENIX) has been conceived to be a front-end device. This means that FENIX is placed between the antenna system and the front-end of a GNSS receiver, and then, it performs the RFI mitigation by excising the undesired RFI signal from the useful GNSS signals with techniques similar to the explored above. It uses a non-parametric algorithm based on a combination of statistical techniques and the MFT, bestowing it with the capability to work against any kind of RFI without prior knowledge of its characteristics.

5.2.1 Current version

The functional block diagram of the system can be divided into two sub-blocks: an external analog RF stage, and an internal digital Signal Processing (SP) stage. The former one conditions the signals collected from the antenna

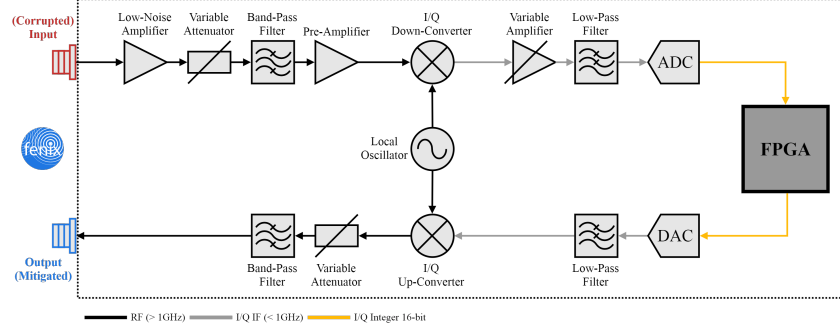


Figure 5.1: FENIX Hardware, Radio Frequency Stage

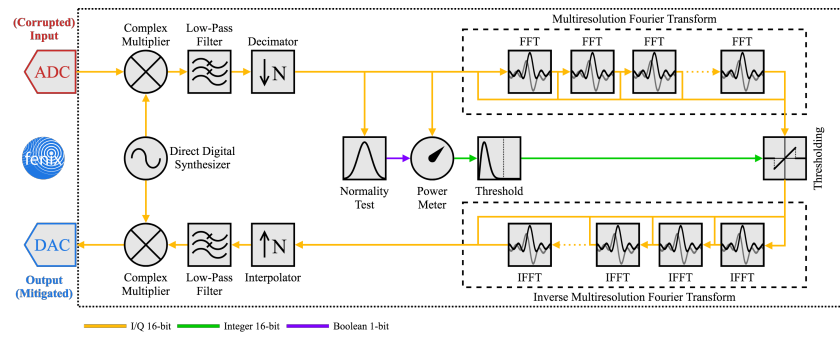


Figure 5.2: FENIX Hardware, Signal Processing Stage

in two separate bands, and delivers them to the receiver; whereas the latter one filters and excises undesired RFI and jamming signals from useful GNSS signals for each of the RF bands.

In the RF stage (Figure 5.1), the signal coming from the antenna (which may be RFI-contaminated or not) is preprocessed for posterior processing in the FPGA. Afterwards, the signal is reconverted back to its original state using the same local oscillator. This process makes FENIX transparent to the receiver, providing increased versatility when compared to other RFI detection and mitigation systems. The processing time inside the FPGA is also kept to a minimum in order to maintain compatibility with GNSS timing applications [29].

The SP stage is completely digital, and it is implemented into an FPGA because of the high throughput, the large number of logic cells, and pipeline architecture needed to implement the FENIX mitigation algorithm. Figure 5.2 illustrates a block diagram of the SP stage.

A Normality test is first applied to the digital data in order to determine if the incoming samples are RFI-contaminated or not (i.e. they follow a Normal distribution or not). Thus, the properties of the signal in the statistical

domain are first used to take the necessary actions in the RFI mitigation process. If the Normality test determines that the decimated Base Band samples are Normal, their power is estimated.

Once the variance of the noise has been estimated, the threshold α can be obtained as a function of the desired probability of false alarm, P_{FA} . Suitable values for P_{FA} for GNSS signals are in the range from 10^{-5} to 10^{-6} [11], because of their spread-spectrum correlation gain.

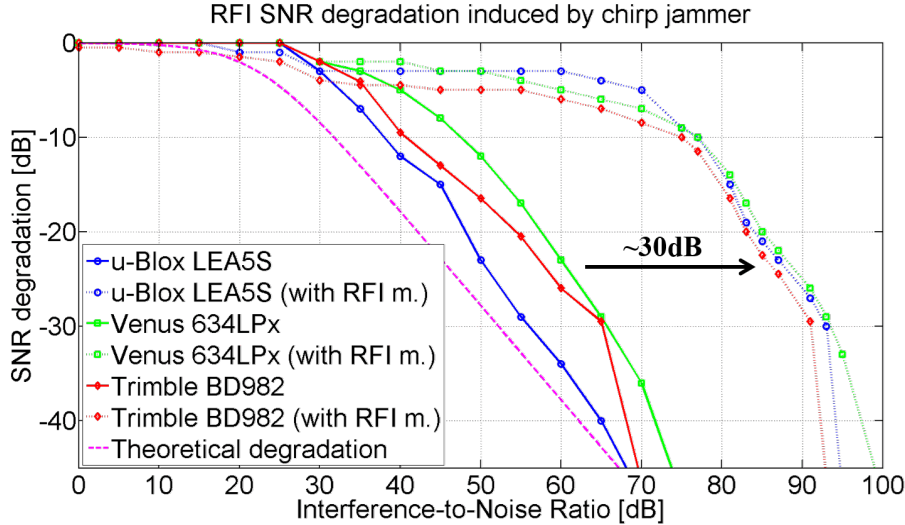


Figure 5.3: Average SNR degradation for multiple GPS commercial receivers. Chirp with 2 MHz bandwidth and 200 Hz of repetition frequency.

Using this approach, FENIX-equipped GNSS systems are capable of improving their SNR degradation by about 30 dB, as shown in Figure 5.3. The performance of FENIX has already been assessed in fields such as Microwave Radiometry [30] and GNSS / GNSS-R, but thanks to the GNSS simulator introduced in Chapter 4, the combined performance will be assessed in the next Section.

5.2.2 FENIX Testing

Using the same testbench introduced in Figure 4.8, the effects of RFI were studied together with the GNSS signal generator. The Signal generator became a perfect enabling technology to test the FENIX outside of the laboratory, as no bulky equipment was needed to perform the test, only SDR. A CW signal (Figure 5.4) was added digitally to the output of the GNSS Signal generator with configurable output levels so as to show the improvement due to the addition of a detection and mitigation system.

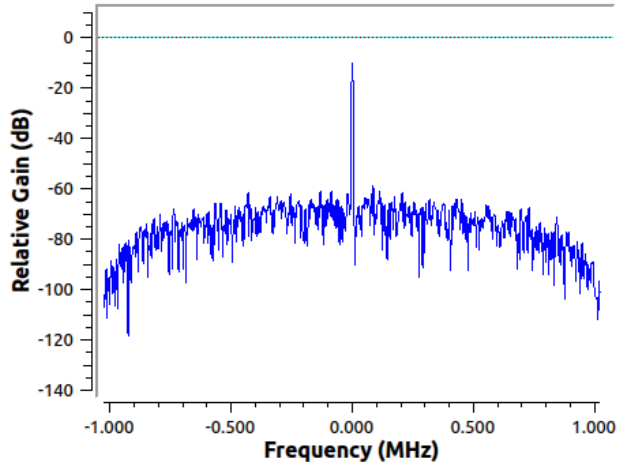


Figure 5.4: Interference signal at -10 dBm

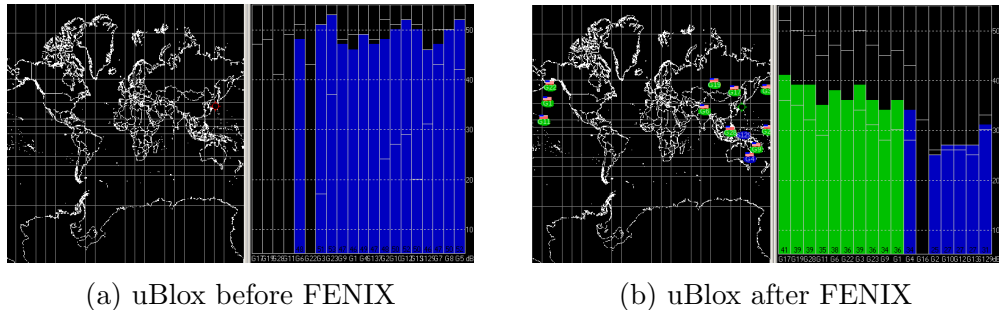


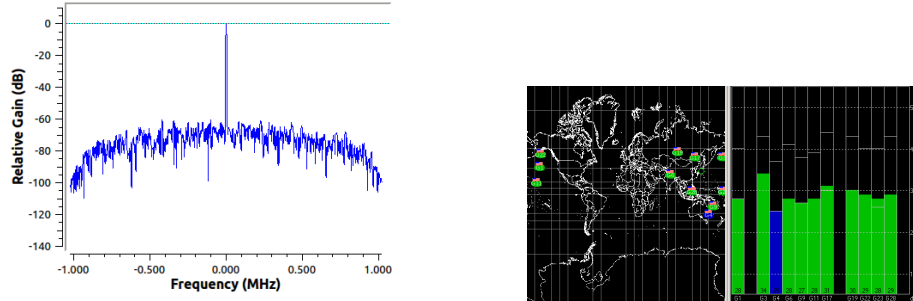
Figure 5.5: Comparison of uBlox performance with and without FENIX

The $C_N/0$ of the satellites decreased linearly with the increase in signal power of the CW signal, until the receiver was unable to maintain lock at an interference level of -10 dBm (Figure 5.5a). After the introduction of FENIX, u-Blox acquired the signal and calculated the position again (Figure 5.5b).

In order to test the gain in Interference-to-Noise Ratio (INR) that FENIX provides, the RFI power was increased (Figure 5.6a) until the upper limit of FENIX was found (Figure 5.6b). With an RFI of 0 dBm, uBlox lost lock again.

RFI is also a field of concern for GNSS-R missions, as it can corrupt valuable scientific data.

In the second part of the test, the same RFI will be introduced into a high dynamics signal with a reflected component. As this signal is processed by the DDM calculator, the effect of FENIX will once more become apparent in recovering the scientific observables.



(a) Interference signal at 0 dBm (b) Upper limit of the FENIX hardware

Figure 5.6: Testing the upper limit of FENIX for this combination of GNSS signal plus interference

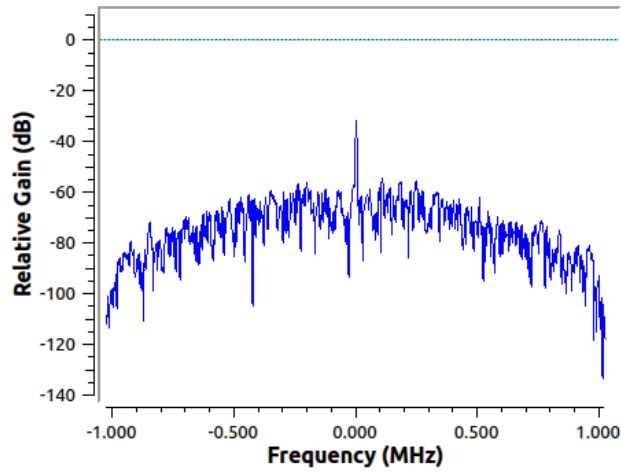


Figure 5.7: Interference signal at -30 dBm

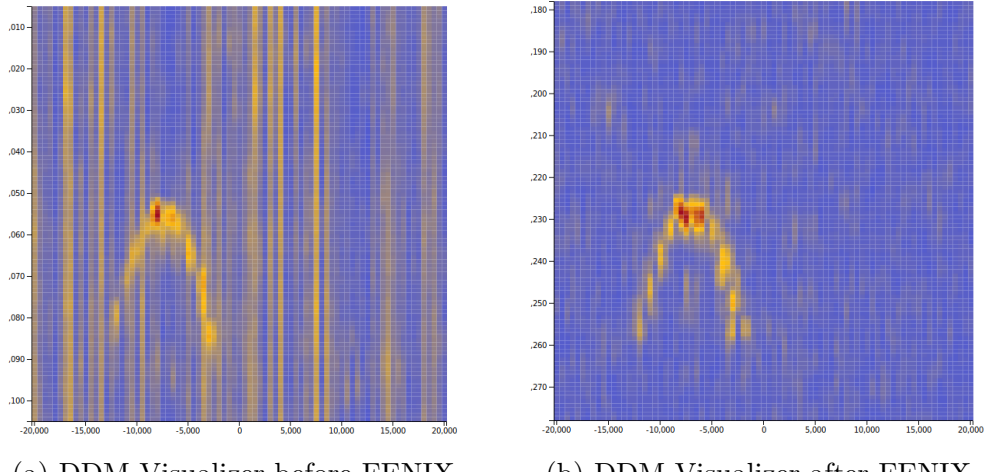
The RFI now has a power of about -30 dBm (Figure 5.7). When the DDM is calculated, vertical lines appear often destroying the horseshoe shape from where physical measurements can be deducted (Figure 5.8a).

After the introduction of FENIX, the vertical lines disappear but the background noise increases (Figure 5.8b).

5.2.3 New version

The current implementation of FENIX suffers from several drawbacks. First of all, it only supports one band due to its implementation in the FPGA of a USRP B205mini, which only has one AD9361 chip.

During the development of this work, a new version of the FENIX (Figure



(a) DDM Visualizer before FENIX (b) DDM Visualizer after FENIX

Figure 5.8: Comparison of DDM observables with and without FENIX

5.9) is being produced using a Xilinx Kintex-7 FPGA and a dual AD9361 configuration, aiming to solve all of the previous problems. The manufacturing, electronic design and idea for this new version were handled by Dr. Querol and Balamis S.L., whereas the implementation of the firmware for software control and bootloading is done by the author.

Automatic gain control is one of the key improvements over the old version. In order to make FENIX work as optimally as possible, the dynamic range needs to be adequate for every combination of GNSS signal plus RFI. A low dynamic range means that the RFI will probably saturate the receiver, and thus the signal processing will not be enough to completely excise the signal. If the dynamic range is too large, the GNSS signal will be hidden beneath the noise.

Adding dual-band capabilities also means that any system using complementary frequency bands (e.g. L1/L2, L1/L5, etc.) will be capable of having both of them excised of RFI at the same time, with the timing synchronization that it ensures.



Figure 5.9: New FENIX in a custom-made enclosure manufactured by Balamis S.L.

CHAPTER 6

Design and implementation of an S-band Ground Station at the Observatori Astròonomic del Montsec

A critical part of every space mission lies in the ability of the ground segment to contact the satellite to transmit telecommands and to receive the scientific yield and/or telemetry data the system has acquired.

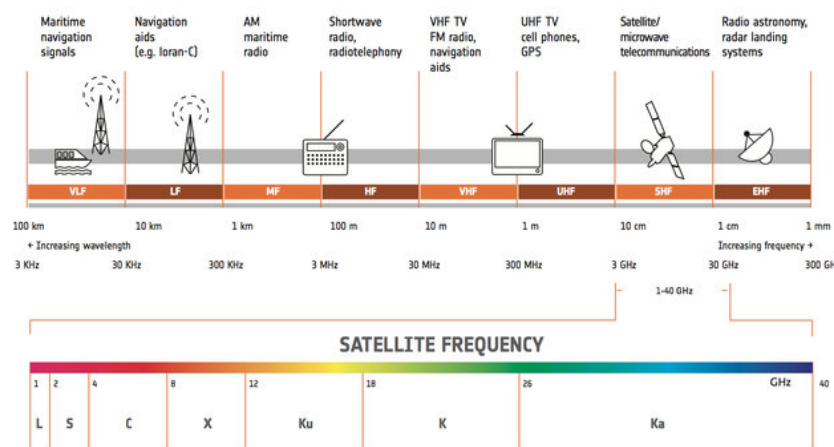


Figure 6.1: Satellite Frequency Bands. Source: ESA

The NanoSat Lab currently operates an UHF / VHF GS in the OAdM. Nowadays, most small satellites use the S-band (2200 - 2290 MHz) for down-link due to its cheaper cost, having no need for precise pointing and wider bandwidth available for data transmission at higher bitrates. Moreover, with the imminent launch of the FSSCat mission [13], the NanoSat Lab was in need for an S-band GS capable of receiving the scientific data the mission will produce. From this need, the new OAdM S-band permanent GS had to be designed and implemented.

6.1 Basic principles of a Ground Station

In order to track a satellite, its path must be previously known by the receiving antenna so as to follow its movement. All satellites are indexed by their North American Aerospace Defense Command (NORAD) Satellite Catalog Number, and websites such as Celestrak distribute TLE Sets that can be used to propagate their orbit and obtain their position at any point in time.

6.2 Design and Link Budget

The main design of a GS is composed of an RF Chain, an Antenna and Azimuth and Elevation rotors that are able to move the Antenna.

All of the aforementioned components are critical to the correct operation of a GS. A misbehaviour in any of these components can make communications impossible. Thus, industrial grade components must be used with long Mean Time to First Failure (MTTF), and the location must be carefully chosen. The emplacement of the GS is critical in the design: in order to avoid interferences found in densely populated cities (as will be discussed in Section 6.3.3), most GSs are located far from civilization. Conversely, it is also beneficial for the GS to be easily accessible by technicians to ensure its continued use. After discussions with the Institut d'Estudis Espacials de Catalunya (IEEC), they agreed to cooperate with us and yield an unused space in the OAdM to host our GS (Figure 6.2).

In order to start the design of a GS, a set of minimum characteristics or requirements has to be compiled. In the case of the Montsec GS, the requirements came through the need of an S-band GS to receive data from the FSSCat mission, and thus the characteristics of the spaceborne transmitter (Table 6.1) guided the initial design.

From the values found in Table 6.1, we can calculate the noise level and received signal power by using the formulas for Free Space Path Losses (FSPL)



Figure 6.2: Future location of the new S-Band in the OAdM

Table 6.1: Transmitter characteristics for the FSSCat mission

EIRP	8 dBW
Frequency Band	S-Band
Bandwidth	5 MHz
Polarization	RHCP
Target E_b/N_0	5 dB

and Noise Level [31].

$$\text{FSPL} = \left(\frac{4\pi d}{\lambda} \right)^2 \quad (6.1)$$

$$P_n = k \cdot T_a \cdot Bw \quad (6.2)$$

where d is the maximum distance of the link, which is around 2000km at the horizon for a LEO satellite, λ is the wavelength of the downlink frequency, k is the Boltzmann constant, T_a is the antenna temperature and Bw is the bandwidth of the signal.

Thus, referring to Table 6.1:

$$\text{FSPL} = \left(\frac{4\pi 2000 \cdot 10^6}{0.132} \right)^2 = 2.760 \cdot 10^{-17} = -165.6 dB \quad (6.3)$$

$$P_n = k \cdot 283.15K \cdot 5e6 = 2.192 \cdot 10^{-8} = -77.09 dB \quad (6.4)$$

$$P_s(dBm) = P_T(dBm) + G_T(dB) + G_R(dB) - L_S(dB) + FSPL(dB) \quad (6.5)$$

$$= 38 + 0 + G_R - 8 - 165.6 \quad (6.6)$$

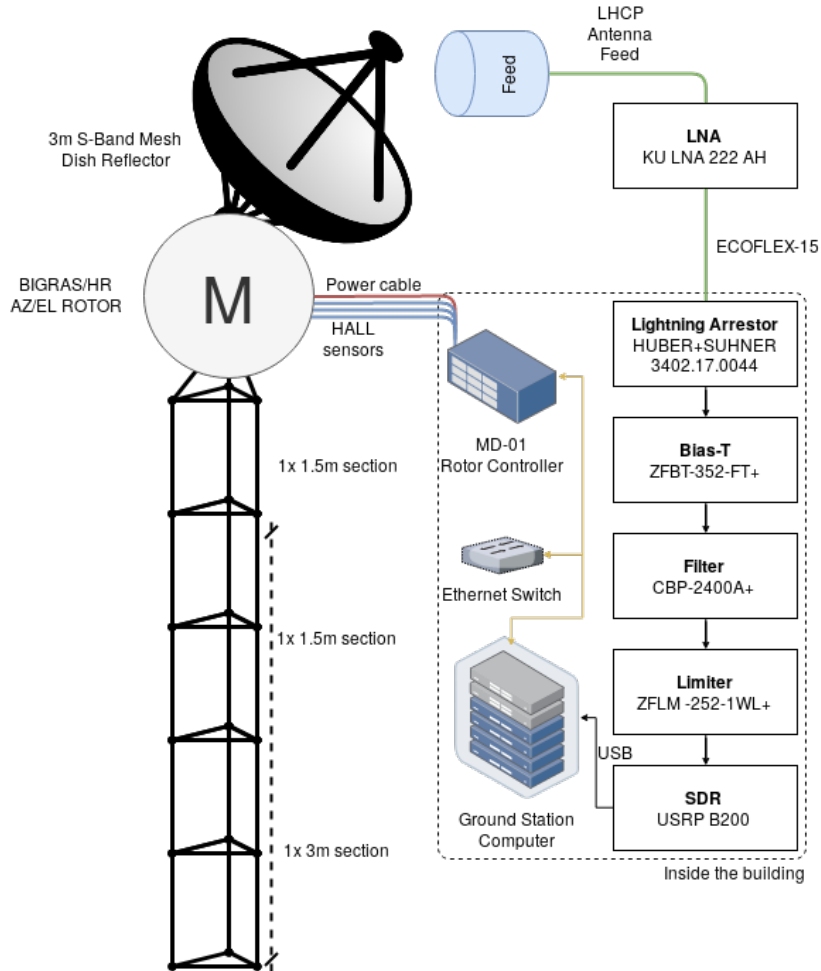


Figure 6.3: Block diagram of the S-Band Ground Station

where P_T is 38 dBm and G_T is supposed 0 dBm as per Table 6.1 and L_S are other system losses that are detailed in the Appendix A.

In order to reach the Target E_b/N_0 , approximately 35 dB of receiver gain are needed. In the following sections, the different parts of the receiver will be discussed, and thus the choices to achieve the Target E_b/N_0 .

6.2.1 RF Chain

The RF chain of a GS includes the components that process the signal and extract useful data from the physical layer. It starts from the antenna feed, and continues until the signal is consumed in a receiver (Figure 6.3). First of

all, an Low-Noise Amplifier (LNA) amplifies the signal received in the feed with a low Noise Figure (NF) as close as possible to it. Due to being the first element in the chain, the LNA's NF sets the NF for the complete chain. This amplification also compensates the losses for the cable that comes after it to reach the needed sensitivity in the SDR. LNAs are usually characterized by four parameters: Frequency range, NF, Gain and Output Third-order Intercept Point (IP3). From a previous installation, the laboratory acquired a Kuhne Electronic KU LNA 222 AH that was no longer in use. With a frequency range of 2200-2400 MHz, 0.5 dB of typical NF, 30 dB of typical Gain and 27 dBm of IP3, this amplifier was a perfect fit for our RF Chain.



Figure 6.4: Cabling diagram

Following the LNA, the next step is to take this amplified signal to the inside of the Telescopi Joan Oró building, where the receiver will be placed. In Figure 6.4 we can see the approximate path the cabling will take, and thus calculate the length of the cables for attenuation purposes. It was decided to use ECOFLEX-15 RF cabling, which provides an excellent attenuation per meter for our frequencies at 0.15 dB/m. This cable will connect the feed of the antenna directly to more equipment inside the Telescopi Joan Oró building, so extra care should be placed to handle electrostatic discharges such as lightning (which are fairly common in the OAdM). Even though the OAdM possesses several lightning rods throughout the whole complex, we decided to add a Lightning Arrestor before the cable enters the building. If the power at its input exceeds a very high limit, the Gas Discharge Tube (GDT) technology redirects this power to the ground to protect the electric equipment that comes after it.

Once inside the building, components that need a power supply can be used. A Bias-T is needed to inject DC voltage into the cable so as to power the LNA at the feed. The main requisite for the Bias-T is for it to have the appropriate voltage for the LNA, which in our case was from 9 to 15V. It is also necessary to use a filter to attenuate any unwanted signals out of the

band of interest, so as to not saturate the input of the SDR. Finally, a limiter is used to constraint the maximum power to the limits of the SDR.

SDRs are understood as "*Radio in which some or all of the physical layer functions are software defined*", and delineates a collection of hardware and software technologies where some or all of the radio's operating functions (also referred to as physical layer processing) are implemented through modifiable software or firmware operating on programmable processing technologies. The use of these systems in a GS allow for digital filtering and processing to be performed on the signal.

Harnessing the power of SDR is done through GNU Radio (GR). GR is a framework that allows users to design, simulate and deploy real-world radio systems in a highly modular and "flowgraph"-oriented way. It contains an extensive library of signal processing blocks, and also allows for the creation of new ones in both the Python and C++ programming languages.

GR allows for complete synchronization, demodulation and decoding schemes to be implemented in software, and updated to meet the needs of any future use of the GS.

6.2.2 Antenna

The antenna is critical for the design of the GS. For this project, a 3 meter parabolic reflector that was purchased for a previous project (Figure 6.5) is used. The reflector dish is made out of a 6.1mm mesh that appears solid to frequencies up to 6 GHz, and makes it more capable of handling strong winds as the surface is perforated whilst also making it nimble enough to only weigh 30kg.

The reflector is accompanied by a feed that harnesses the power gathered by it. One of the most important characteristics is its polarization. Most S-Band transceivers work with Right-Handed Circular Polarization (RHCP), but as the feed receives the signal after reflecting off the dish, its polarization must be Left-Handed Circular Polarization (LHCP). The bandwidth must be located within the S-band downlink (2200 - 2290 MHz), and thus exhibit low Voltage Standing Wave Ratio (VSWR).

At S-band, this reflector has a gain of 35.4 dB, and a 3 dB beam width of 3.2° as per the manufacturer's measurements. The gain of the feed is not added to the gain of a dish. The purpose of the feed is to receive all possible RF energy from the dish, without receiving spurious energy from beyond the dish edges. If the feed is correctly placed, the gain of the dish is sufficient so that the missing signal power in Section 6.2 is compensated.



Figure 6.5: 3m Dish Reflector on top of the Campus Nord D3 building's roof

6.2.2.1 Wind load calculation

In order to install a reflector of these dimensions at an emplacement with strong winds such as the OAdM, a study on the effects of wind in both the antenna and the rotor has to be performed. Strong winds can not only endanger the antenna and neighboring structures, but it is also critical due to the narrow beamwidth of the reflector that the rotor is capable of maintaining pointing.

The historical data for wind speed can be obtained from the OAdM's website (Figure 6.6).

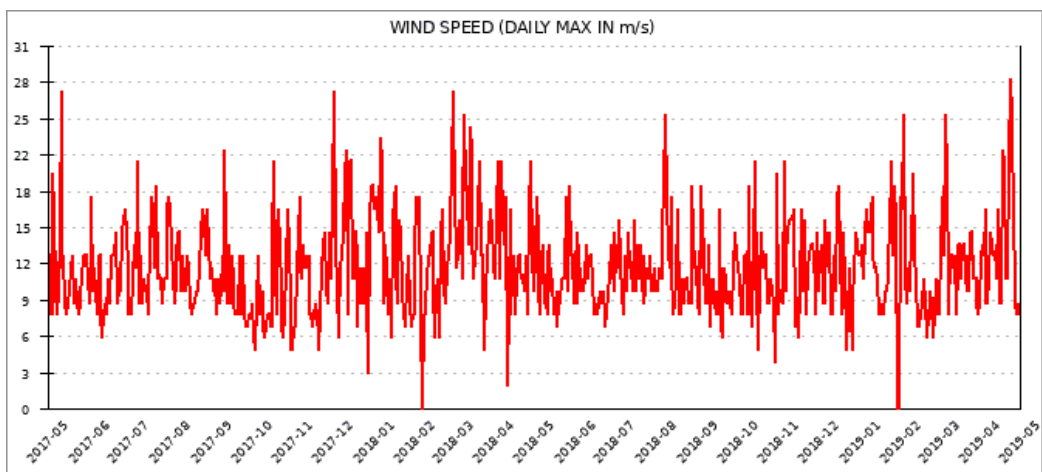


Figure 6.6: Maximum Wind Speeds (2y) at the OAdM. Source: iec.cat

Together with the specifications obtained from the manufacturer (Figure 6.7), we can calculate the maximum torque the antenna will be subjected to.

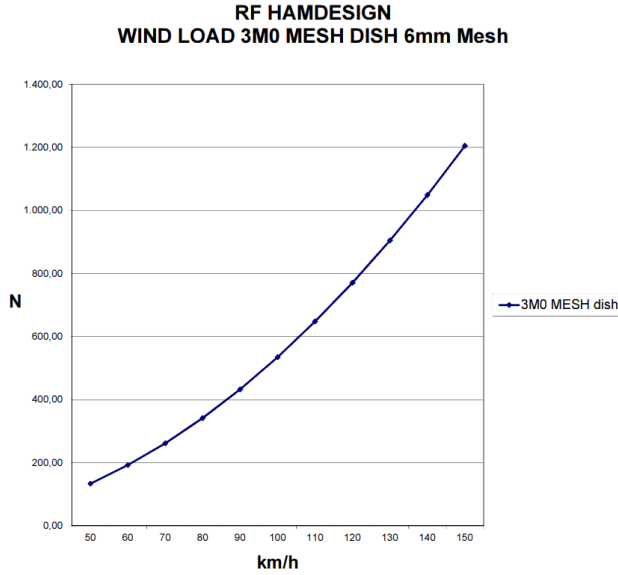


Figure 6.7: Wind Load graph for the 6mm mesh antenna. Source: rfhamdesign.com

The wind speed has been shown to never surpass 28 m/s (100.8 km/h), which using the specifications for the antenna would give us a maximum force of around 570 N if received frontally with the largest possible area. Taking into account a safety margin of 100%, it would translate to 1040 N of force at the worst possible case, including the antenna being completely unsheltered from the wind by the surrounding buildings, as the aforementioned wind readings are performed at sufficient height such that none of the buildings can interfere with the wind.

For this reason, a rotor capable of withstanding such force would be needed to properly drive this antenna. For the spinning force caused by the antenna to the rotor while braking, the worst case scenario of one of the halves of the antenna being hit by very strong winds is considered. This would amount to roughly 500 N of force applied to half of the antenna, of which the farthest point would be located at a distance of 1.5 m of the turning axis. This would be translated to a torque of

$$500\text{N} \cdot 1.5\text{m} = 750\text{N} \cdot \text{m} \quad (6.7)$$

For typical wind speeds of around 12 m/s (43.2 km/h), the exerted force would be of 100 N . Taking into account the worst case scenario mentioned

before, that would result in

$$200N \cdot 1.5m = 300N \cdot m \quad (6.8)$$

These values will help to choose a suitable rotor in the next Section.

6.2.3 Rotor

The rotors move the antenna so as to track the satellite, keeping it inside the antenna beamwidth. Smooth movement is needed to avoid jerks that might cause a loss of reception due to the narrow beamwidth. It is then necessary to acquire a rotor that is capable of keeping up with the satellite position without introducing jerking, and also to move even with the resistance suffered from strong winds.

Some of the requirements for the rotor have been laid out in previous sections. From the wind load calculation, a rotor with at least 450Nm of braking torque and 75Nm of moving torque should work in the OAdM. From the reflector, it is known that for the used frequencies, the beam width is around 3°. The rotor must then be capable of moving with as much resolution as possible, always within at least 1.5° of precision so as to not have periodic signal losses.

The SPID BIG-RAS/HR is capable of $610N \cdot m$ of turning torque, as well as $2.712 N \cdot m$ of braking torque. It is then capable of overcoming both cases with its turning torque, and thus capable of moving the antenna while the brakes are not applied, keeping its pointing accuracy. It also boasts an impressive 0.1 degrees of resolution, being able to move freely within the 3° beamwidth of the antenna.

This rotor was supplied with a mounting bracket (Figure 6.8) that allowed for counterweights to be used, increasing even more the stability of the setup. In order to calculate the suitable counterweights for the antenna plus rotor contraption, we have to take into account the distances and weights of all the elements in relation to the pivot point on which the rotor will rest. This is the same as saying that the torque (τ) on both sides of the antenna has to be equal for the system to be in equilibrium, as seen in Figure 6.9.

Torque is calculated as follows:

$$\tau = F \cdot d \quad (6.9)$$

$$F = m \cdot a \quad (6.10)$$

where F is Force in N, d is distance to the pivot point in meters, m is mass in kg, and a is the acceleration of the object, in m/s². By using our values,



Figure 6.8: UA-02 Heavy Duty bracket plus BIG-RAS/HR

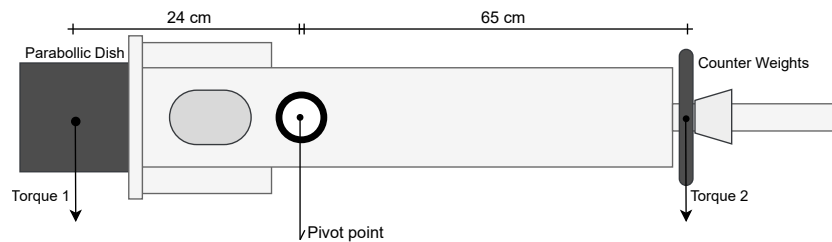


Figure 6.9: Counter Weight calculation

we obtain:

$$\tau_1 = F_1 \cdot d_1 \quad (6.11)$$

$$\tau_2 = F_2 \cdot d_2 \quad (6.12)$$

$$\tau_1 = \tau_2 \quad (6.13)$$

$$F_1 \cdot d_1 = F_2 \cdot d_2 \quad (6.14)$$

$$30 \cdot G \cdot 0.24 = x \cdot G \cdot 0.65 \quad (6.15)$$

where G is the standard gravity (9.80665 m/s^2).

$$x = \frac{30 \cdot G \cdot 0.24}{0.65 \cdot G} \quad (6.16)$$

$$x \approx 11 \text{ kg} \quad (6.17)$$

Thus, we opted to buy two 5 kg commercial weights to place them on each arm of the bracket.

In order to control the rotor, an Ethernet-enabled rotor controller was supplied. This controller is capable of performing *soft-start* and *soft-stop*, meaning that the rotor will ramp up the power when moving or braking so as to eliminate the jerking that affected other rotors with a reflector as big as this one.

By implementing the Rot2Prog protocol [32], it is possible to control the rotor from any software, such as the ground station controller, which will be detailed in Section 6.2.4.

6.2.4 Software

In order to control the GS, a new software architecture was designed together with an Operation Center (OC). GSs are bound to be controlled remotely as they usually are located in hard to reach locations. It is also interesting to be able to control many GSs at once to maximize coverage and thus pass opportunities.

The control software was designed with this in mind, and provides a common interface to each GS with a different adapter for each to handle internal specificities. A distributed architecture with modular design is being developed in the NanoSat Lab to act both as the control software for the GS and as the Operations Center. A diagram can be found in Figure 6.10.

The Application Programming Interface (API) for each GS is capable of performing all the common tasks such as scheduling passes for that GS, doing maintenance, manually moving the rotors, etc. The OC can communicate with those APIs to orchestrate a vast array of GSs, and also keeps track of every scheduled pass on its own database for redundancy.

This software is still being developed mainly by Ms. Aina Garcia as the main contribution of her Degree's Thesis, and is out of the scope of this work, but an adapter for the Montsec S-Band GS was developed in order to test and operate it.

6.3 Testing

In order to test the complete GS before delivering it to the OAdM, a provisional version was built on top of the D3 building in Campus Nord.

6.3.1 Assembly

First of all, the rotor was connected to the controller through 4 different cables. 3 of them were for the HALL sensors that indicate the current Azimuth

System diagram v0.1

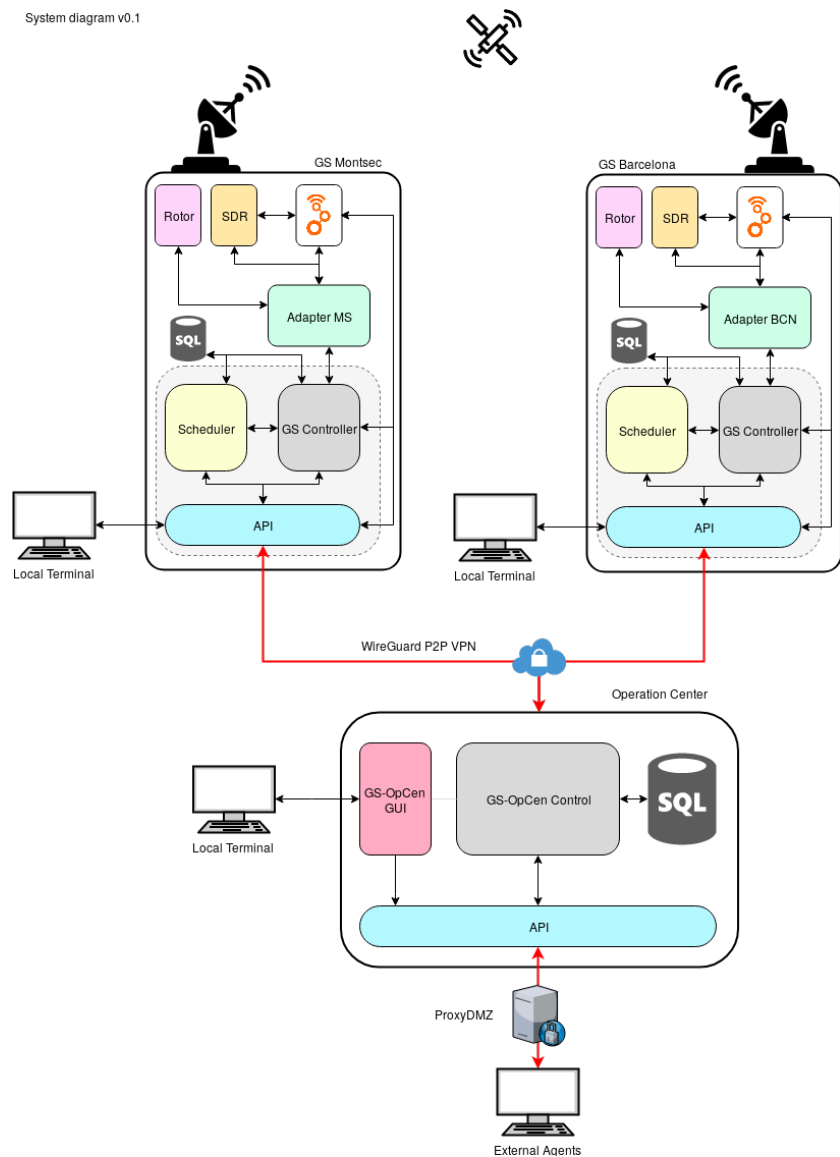


Figure 6.10: Block diagram of the software architecture

and Elevation of the rotor, and the other one was for controlling the rotor's movement through pulsed signals from the controller.

The feed was placed on the reflector, and the LNA + ECOFLEX cable were connected to it. Afterwards, the feed was secured to the rotor through the mounting bracket. Once the Rotor plus antenna contraption was finished, it was mounted on the tip of the 6 meters mast, that was laying flat. The



Figure 6.11: Hoisting the antenna

mast was raised by means of a hoist, as seen in Figure 6.11. It was then secured with guy lines to three anchor points, and to the ground with M16 threaded rods. The complete assembly can be seen in Figure 6.12a.

The cables were connected to the rack enclosure inside the building (Figure 6.12b), where the rest of the RF Chain resided. A quick test was performed by moving the rotor manually using the controller, and the soft-start/stop system managed to move the antenna smoothly without sudden jerks. Calibration of the rotor are discussed in Section 6.3.2.

The spectrum was also monitored using a Spectrum Analyzer, and the results are discussed in Section 6.3.3.

6.3.2 Calibration

There are several calibrations that have to be performed on an antenna to ensure correct pointing.

6.3.2.1 Elevation

The BIG-RAS/HR rotor has mechanical stops in elevation in order to be capable of resting the antenna when stopped. These stops are located at 0° and



(a) Finished antenna



(b) Rotor controller and PSU



(c) Detail of the antenna

Figure 6.12: Complete assembly at the roof of D3 building

180°. Thus, it is important to let the rotor move until one of the mechanical stops are found before inserting the elevation pipe with the mounting bracket. To calibrate elevation, if the mast is already calibrated, a simple accelerometer or spirit level can be used while the rotor is laying sideways. By measuring at the mast's tip with a spirit level prior to performing this calibration, either calibration can be ensured, or the offset to be applied can be extracted for the rotor's calibration.

6.3.2.2 Azimuth

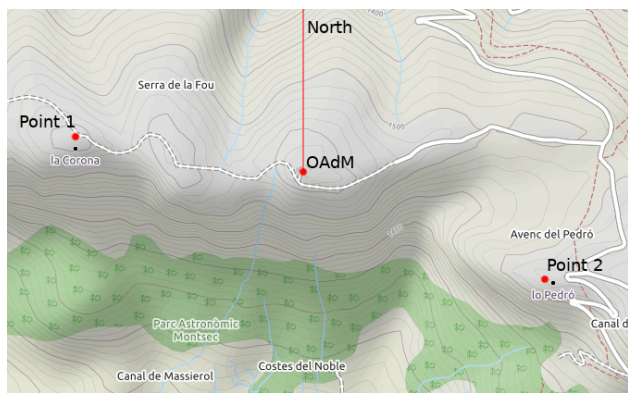


Figure 6.13: Proposed measurement points for Azimuth Calibration

Calibrating Azimuth can be done via software, as the rotor can move past 360°. Several reference points can be taken by pointing the antenna towards known signals, and thus the azimuth can be calibrated by plotting all the reference points in a map (Figure 6.13), together with the angles for each measurement. Assisted by a GPS receiver, a simple transmitter can be set in the marked locations to serve as reference points.

6.3.2.3 Feed

It is also important in order to harness all the energy gathered at the reflector to correctly aim the feed at the center. A simple practical way to find the focus of any dish is to secure mirrors on the surface of the reflector, aim the dish at the Sun, and find where the reflections converge to place the feed.

6.3.3 Interferences

During the tests in Barcelona, we identified strong RFI from UMTS signals. When an amplifier or other circuit becomes non-linear, it will begin to pro-

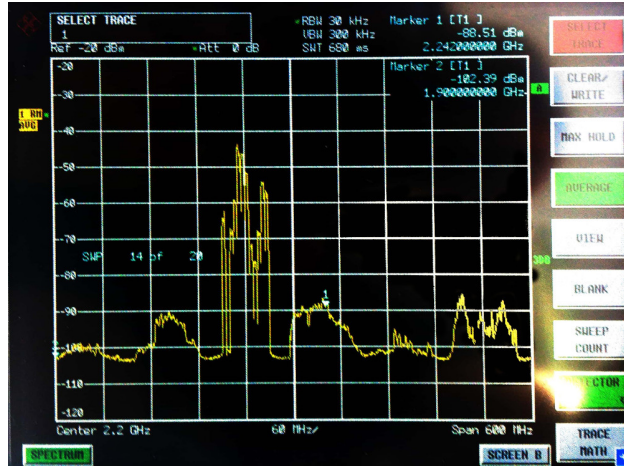


Figure 6.14: Intermodulation Products received in Campus Nord (2.2 GHz center, 600 MHz span)

duce harmonics of the amplified inputs. Non-linearity will also produce a mixing effect of two or more signals. If the signals are close together in frequency, some of the sum and difference frequencies called intermodulation products produced can occur within the bandwidth of the amplifier. This RFI covered the whole S-band spectrum, as seen in (Figure 6.14).

It is possible that the transmitting amplifiers used in UMTS base stations such as the one at *Cuartel del Bruch* have low IP3 values that cause intermodulation products at the output.

Part of the problem was caused by the feed that was used, as it did not have a choke ring to eliminate the secondary lobes that captured RFI at these frequencies. One of the solutions could be to add a cavity filter at the input. During a preliminary trip to Montsec, measurements of the spectrum were taken for possible interferences (both from a new Radio Link by Endesa and UMTS signals). As no RFI was found, there was no need for adding a cavity filter that could add extra attenuation before the LNA. As is seen in Chapter 5, RFI mitigation is critical nowadays due to the amount of RF that is being transmitted continuously.

6.4 Installation in the OAdM

After testing in Barcelona, the next step was to install the GS in its final destination at the OAdM, as seen in the render in Figure 6.15a. It was decided to use the building as a support for the antenna due to the strong winds found in the OAdM, as seen in Figure 6.6. Thus, the assembly had to

be modified to account for this change.



(a) Sketch of the final assembly (b) Foundations laid

Figure 6.15: Render of the final installation in the OAdM, next to the already laid foundations

A preliminary trip to the Montsec OAdM was done in the middle of May 2019, and the foundations for the final installation were laid. The reinforced concrete in the ground was perforated with an M18 drill, and threaded rods were inserted using chemical anchoring. The rods fit tightly to the holes in the plate, and were secured with nuts.

In order to act as guy lines and to bear the brunt of the shearing forces caused by the winds, four wall-mounted anchorings were installed. Instead of securing them to the wall with wall anchors, threaded rods larger than the wall were used, and using washers at the other side they were tightened.

The completed foundations can be seen in Figure 6.15b.

6.5 Conclusions and Future Work

The design and construction of a functioning GS is a complex task requiring knowledge of the entire system, from the ground segment to the space segment. Each of the parts must work in unison, extensive testing has to be performed to each of them, and the cost for high-end components is usually

prohibitive. Nowadays, with the introduction of SDR, a big part of the RF Chain can be implemented in software, thus relaxing the requirements for critical components such as amplifiers or antennas.

Upgrades to the current design of the GS include automatic calibration equipment (for azimuth and elevation) and the addition of more frequency bands that are becoming widely used. In case of a possible upgrade to also act as a transmitter within S-Band, several options are available:

- To use the same feed for both uplink and downlink, doing so in Half-Duplex mode (only uplink or downlink at the same time). In order to do this, a feed with a bandwidth spanning 2025 - 2290 MHz must be found, which is rare and costly.
- To use a dual band feed with two different connectors. One of them is centered at uplink, and the other at downlink. If the isolation between ports is good enough, this would allow for Full-Duplex.
- Using a Bidirectional Amplifier with power detection, triggering a physical switch to access the antenna when in transmission mode.

For now, this GS is planned to be receive-only, so a single band feed has been purchased and installed.

As the installation in the OAdM was not completed prior to the finalization of this work, an additional 2-day trip will be performed during June 2019 to complete the construction of the GS. Afterwards, the GS will be tested for several months until the launch of the FSSCat mission.

CHAPTER 7

Conclusion and Future Research

This work has shown the importance of preparation and simulation for any RS mission. Simulating the environment as closely to reality as possible is key to understand the performance of the system, and avoid any potential pitfalls.

In Chapter 3, a comprehensive study on the effects of high dynamics in GNSS receivers was performed. It is important to understand the limitations of such receivers (COCOM limits, bandwidths...), as an unknown factor could jeopardize the entire mission if unprepared for.

The current limitations of existing equipment also prompted for the creation of a custom GNSS and GNSS-R signal generator in Chapter 4. This allowed for testing several technologies such as a GNSS-R EO payload (DDM Calculator, with the help of Mr. Joan Francesc Muñoz), and a GNSS RFI mitigator (FENIX).

The DDM Calculator was proven to accurately and efficiently obtain GNSS-R observables from simulated and real signals, and will fly in the FSSCat mission. Performance tests showed that RFI mitigation systems are a welcome inclusion in any kind of GNSS or GNSS-R mission that is susceptible to suffer performance degradation due to RFI.

The hardware choices and design for the Montsec S-band GS were proven to be correct during testing. Even though the software is still under heavy development, it is expected to reduce human error and to provide automated ways to schedule passes and obtain telemetry and scientific yields.

As for future improvements, the work made in high dynamics receivers could be expanded with the inclusion of Kalman filters, that are now getting to the point of being able to be run efficiently in current spaceborne hard-

ware. The GNSS simulator could also be used to repeat the tests and obtain smoother Doppler curves, more closely resembling reality.

The GNSS simulator is already becoming an indispensable tool for testing new technologies, and is under heavy development to add more accurate models and performance optimizations. Precise ionospheric modellings are critical for the correct behaviour of GNSS systems, and thus are a priority in the development of future versions.

Work on the new version of the FENIX is underway, and will improve on the performance of the previous version, as well as exhibit extended capabilities. As no continuous monitoring of the input signal power is being done, the gains, which are manually introduced during runtime, may not be optimally chosen at every moment. Improving this behaviour is one of the main points of the new version that is being created together with Dr. Querol.

With regard to the Montsec S-band GS, it is expected to be finished in early June 2019, and testing will begin shortly after. A future improvement could be to add the capability for uplink in S-band, and/or other commercially used bands. Thanks to the modularly programmed software, it is also possible to add new GSs to the network with very little cost, as the software is reusable and the hardware design is already done.

Bibliography

- [1] Estel Cardellach, Jens Wickert, Rens Baggen, Javier Benito, Adriano Camps, Nuno Catarino, Bertrand Chapron, Andreas Dielacher, Fran Fabra, Greg Flato, Heinrich Fragner, C Gabarro, Christine Gommenginger, Christian Haas, Sean Healy, Manuel Pajares, Per Høeg, Adrian Jaggi, Juha Kainulainen, and Cinzia Zuffada. Gnss transpolar earth reflectometry exploring system (g-tern): Mission concept. *IEEE Access*, PP:1–1, 03 2018. doi: 10.1109/ACCESS.2018.2814072.
- [2] J. Puig-Suari, C. Turner, and W. Ahlgren. Development of the standard CubeSat deployer and a CubeSat class PicoSatellite. In *2001 IEEE Aerospace Conference Proceedings (Cat. No.01TH8542)*, volume 1, pages 1/347–1/353 vol.1, March 2001. doi: 10.1109/AERO.2001.931726.
- [3] Spire. Data & Analytics from Orbit, 2019. <https://www.spire.com/en/spire/about-spire>.
- [4] J. Muñoz, N. Miguélez, R. Castella, L. Fernandez, A. Solanellas, P. Via, and A. Camps. 3Cat-4: combined GNSS-R, L-Band radiometer with RFI mitigation, and AIS receiver for a I-Unit Cubesat based on software defined radio. In *IEEE International Geoscience and Remote Sensing Symposium*, pages 1063–1066. Institute of Electrical and Electronics Engineers (IEEE), Jul 2018. doi: 10.1109/IGARSS.2018.8519037. URL <http://hdl.handle.net/2117/128900>; <https://ieeexplore.ieee.org/document/8519037>.
- [5] European Space Agency. ESA - Fly Your Satellite, 2019. https://www.esa.int/Education/CubeSats_-_Fly_Your_Satellite.
- [6] V. U. Zavorotny, S. Gleason, E. Cardellach, and A. Camps. Tutorial on remote sensing using gnss bistatic radar of opportunity. *IEEE Geoscience and Remote Sensing Magazine*, 2(4):8–45, Dec 2014. ISSN 2168-6831. doi: 10.1109/MGRS.2014.2374220.

- [7] IEEE GNSS+R 2019. Specialist Meeting on Reflectometry using GNSS and other Signals of Opportunity, 2019. <http://www.gnssr2019.org/>.
- [8] The Osmocom project. osmo-fl2k: Using cheap USB 3.0 VGA adapters as SDR transmitter, 2019. <https://osmocom.org/projects/osmo-fl2k/wiki/Osmo-fl2k>.
- [9] R. Oliva, E. Daganzo, Y. H. Kerr, S. Mecklenburg, S. Nieto, P. Richaume, and C. Gruhier. Smos radio frequency interference scenario: Status and actions taken to improve the rfi environment in the 1400–1427-mhz passive band. *IEEE Transactions on Geoscience and Remote Sensing*, 50(5):1427–1439, May 2012. ISSN 0196-2892. doi: 10.1109/TGRS.2012.2182775.
- [10] Philippe Richaume, Yan Soldo, Eric Anterrieu, Ali Khazaal, Simone Bircher, Arnaud Mialon, Ahmad Al Bitar, Nemesio Rodriguez-Fernandez, Francois Cabot, Yann Kerr, and Ali Mahmoodi. Rfi in smos measurements: Update on detection, localization, mitigation techniques and preliminary quantified impacts on soil moisture products. 07 2014. doi: 10.1109/IGARSS.2014.6946397.
- [11] J. Querol Borràs. *Radio frequency interference detection and mitigation techniques for navigation and Earth observation*. PhD thesis, Universitat Politècnica de Catalunya. Departament de Teoria del Senyal i Comunicacions, 2018. Disponible en: <http://hdl.handle.net/2117/125028>.
- [12] Amazon Web Services. AWS Ground Station, 2019. <https://aws.amazon.com/ground-station>.
- [13] A. Camps, A. Golkar, A. Gutiérrez, J. Ruiz de Azúa, J. Muñoz, L. Fernandez, C. Diez, and A. Aguilera. FSSCAT, the 2017 Copernicus Masters’ “ESA Sentinel Small Satellite Challenge” Winner: A Federated Polar and Soil Moisture Tandem Mission Based on 6U Cubesats. In *IEEE International Geoscience and Remote Sensing Symposium*, pages 8285–8287. Institute of Electrical and Electronics Engineers (IEEE), Jul 2018. doi: 10.1109/IGARSS.2018.8518405. URL <http://hdl.handle.net/2117/127836>; <https://ieeexplore.ieee.org/document/8518405>.
- [14] Alex Birklykke. *High Dynamic GPS Signal Acquisition: A Case Study in GPS Receivers on Nano-Satellites in LEO*. Phd thesis, Aalborg University, 2010.

- [15] Elliott D. Kaplan and Chris Hegarty. *Understanding GPS: Principles And Applications*. Artech House, 11 2005. ISBN 1580538940, 978-1580538947.
- [16] Kai Borre, Dennis M. Akos, Nicolaj Bertelsen, Peter Rinder, and Søren Jensen. *A Software-Defined GPS and Galileo Receiver: A Single-Frequency Approach*. Birkhäuser Basel, 01 2007. ISBN 978-0-8176-4390-4.
- [17] Phillip W Ward. Performance comparisons between FLL, PLL and a novel FLL-assisted-PLL carrier tracking loop under RF interference conditions. In *ION GPS-98*, pages 783–795, 1998.
- [18] GNSS-SDR: An open source Global Navigation Satellite Systems software-defined receiver. <https://gnss-sdr.org/>, 2019.
- [19] Realtek RTL2832U. <https://www.realtek.com/en/products/communications-network-ics/item/rtl2832u>, 2019.
- [20] R&S SMU200A Vector Signal Generator. https://www.rohde-schwarz.com/us/product/smu200a-productstartpage_63493-7555.html, 2019.
- [21] Spirent. <https://www.spirent.com/go/what-is-a-gps-simulator>, 2019.
- [22] Scott Gleason, Demoz Gebre-Egziabher, and Demoz Gebre Egziabher. *GNSS Applications and Methods*. Artech House, 7 2009. ISBN 1596933293.
- [23] NGA Geomatics - WGS84. <http://earth-info.nga.mil/GandG/update/index.php?dir=wgs84&action=wgs84>, 2019.
- [24] V. U. Zavorotny and A. G. Voronovich. Scattering of gps signals from the ocean with wind remote sensing application. *IEEE Transactions on Geoscience and Remote Sensing*, 38(2):951–964, March 2000. ISSN 0196-2892. doi: 10.1109/36.841977.
- [25] J. F. Marchan-Hernandez, A. Camps, N. Rodriguez-Alvarez, E. Valencia, X. Bosch-Lluis, and I. Ramos-Perez. An efficient algorithm to the simulation of delay-doppler maps of reflected global navigation satellite system signals. *IEEE Transactions on Geoscience and Remote Sensing*, 47(8):2733–2740, Aug 2009. ISSN 0196-2892. doi: 10.1109/TGRS.2009.2014465.

- [26] Nuand. <http://www.nuand.com/>. bladeRF manufacturer.
- [27] u-Blox LEA-6 Series. <https://www.u-blox.com/en/product/lea-6-series>, 2019.
- [28] S.M. Kay. *Fundamentals of Statistical Signal Processing: Detection theory*. Prentice Hall Signal Processing Series. Prentice-Hall PTR, 1998. ISBN 9780135041352. URL <https://books.google.es/books?id=vA9LAQAAIAAJ>.
- [29] J. Querol, A. Camps, E. G. Manfredini, and R. Píriz. An anti-jamming system for gnss timing applications. In *2018 European Frequency and Time Forum (EFTF)*, pages 155–158, April 2018. doi: 10.1109/EFTF.2018.8409021.
- [30] J. Querol, R. Onrubia, A. Alonso-Arroyo, D. Pascual, H. Park, and A. Camps. Performance assessment of time–frequency rfi mitigation techniques in microwave radiometry. *IEEE Journal of Selected Topics in Applied Earth Observations and Remote Sensing*, 10(7):3096–3106, July 2017. ISSN 1939-1404. doi: 10.1109/JSTARS.2017.2654541.
- [31] Ieee standard for definitions of terms for antennas. *IEEE Std 145-2013 (Revision of IEEE Std 145-1993)*, pages 1–50, March 2014. doi: 10.1109/IEEESTD.2014.6758443.
- [32] SPID Rot1Prog and Rot2Prog Protocol. <http://ryeng.name/blog/3>, 2019.

Appendices

APPENDIX A

S-Band Downlink Link Budget

II

Parameter	Value	Units
Physical parameters		
Frequency:	2270	MHz
Wavelength	0,1321585903	m
Link Distance	2000	km
Bandwidth	5	MHz
Transmitter		
Transmitted Power	38	dBm
Transmitter Antenna Gain	0	dB
Transmitter pointing losses	3	dB
Losses		
Free Space Losses	-165,59	dB
Fade Margin	5	dB
Polarization losses	0	dB
Antenna		
Receiver Antenna Gain	35	dB
Receiver LNA Gain	30	dB
Receiver LNA NF	0,5	dB
Antenna Temperature	10	°C
Target Eb/N0	5	dB
RF Chain		
Cable length	35	m
Cable losses	0,15	dB/m
Parameter	Value	Units

Gain due to:	
Transmitted Power	38
TX Antenna Peak Gain (dB)	0
Transmitter Total Gain (dB)	38
RX Antenna Peak Gain (dB)	35
LNA Gain (dB)	30
Receiver Total Gain (dB)	65

Received Power	-70,59
Noise Power	-76,59
SNR (dB)	6,00
SDR Rx Power	-75,84

Losses due to:	
TX Pointing Losses (dB)	3
Transmitter Total Losses (dB)	3
Free Space Path Loss (dB)	-165,59
Fade Margin (dB)	5
Polarization Losses (dB)	0
Path Total Losses (dB)	-170,59
Cable Losses (dB)	5,25
Cable Total Losses (dB)	5,25

Noise:	
Noise Figure (dB)	0,5
Equivalent temperature (Te) (K)	35,39
Antenna Temperature (Ta) (K)	283,15
Bandwidth (MHz)	5
Noise Power (dBm)	-76,59

APPENDIX B

Budget

Table B.1: Budget of S-band Ground Station

Item	Comments	Price/Qty	Qty	Price
3-Meter S-Band Dish	Parabolic Dish	€1.100	1	€1.100
BIG-RAS/HR	Rotor	€1.536,36	1	€1.536,36
MD-01	incl. w/ rotor	€0	1	€0
MD-01 Ethernet	Ethernet module	€49,59	1	€49,59
Control Cable	4c cable	54,55 €/25m	50 m	€109,1
Sensor Cable	8c shielded cable	56,2 €/25m	50 m	€112,4
UA-02 Bracket	Counterweight	€395,87	1	€395,87
PS-01	Power Supply	€401,65	1	€401,65
LHCP Feed	Antenna feed	€110	1	€110
KU LNA 222 AH-842	LNA at Antenna	€368,60	1	€368,60
ECOFLEX-15	RF Cable	6,97 €/m	40 m	€278,80
ZFBT-352-FT+	Bias-Tee	€112	1	€112
CBP-2400A+	Filter	€33	1	€33
ZFLM -252-1WL+	Limiter	€52	1	€52
TOTAL				€2.356,40